



# Figures of merit and screening approaches for evaluating heat generation in magnetic nanoparticles for hyperthermia

Hiroaki Mamiya<sup>a,\*</sup>, Balachandran Jeyadevan<sup>b</sup>, Eiji Kita<sup>c</sup>, Reisho Onodera<sup>d</sup>, Tetsushi Taguchi<sup>a</sup>, Nikita Kulesh<sup>a</sup>, Hossein Sepehri Amin<sup>a</sup>

<sup>a</sup> National Institute for Materials Science, Japan

<sup>b</sup> Tohoku Univ, Japan

<sup>c</sup> Univ. Tsukuba, Japan

<sup>d</sup> Nat. Inst. Tech., Ibaraki College, Japan

## ARTICLE INFO

### Keywords:

Hyperthermia treatment  
Magnetic nanoparticles  
Magnetic heating efficiency  
Specific absorption rate  
Blocking temperature  
Switching field distribution  
Predictive screening method

## ABSTRACT

The heating performance of magnetic nanoparticles for hyperthermia is conventionally evaluated using the specific absorption rate ( $SAR_{\text{nano}}$ ), measured under irradiation conditions specific to each laboratory. However, because  $SAR_{\text{nano}}$  depends strongly on magnetic field amplitude and frequency, values obtained under non-identical conditions may not serve as a fair metric for comparing material performance. This study examines additional indicators, including the heating selectivity ratio between normal tissue and nanoparticles, which reflects side effects, and the specific power factor, which represents device load (equivalent to the specific absorption rate and intrinsic loss power). The results show that the ratio of experimentally generated heat to theoretical maximum heat output provides a more reliable measure of heat generating efficiency, independent of irradiation conditions. Furthermore, conventional measurement conditions often differ from those that maximize heating performance, potentially excluding nanoparticles with high potential. Therefore, a method is introduced to predict heating behavior over a wide parameter range using the blocking temperature and switching magnetic field distribution. For sparsely immobilized nanoparticles, the predicted values were found to be in good agreement with the experimental results, demonstrating that the method can predict the maximum potential of heat generation performance under ideal conditions. On the other hand, the current method could not adequately account for dipolar interactions or particle rotations; hence, further improvements are needed for applications such as nanoparticles concentrated within endosomes. The proposed performance indicators and predictive framework provide a more robust method for evaluating heating performance, thereby accelerating the development of magnetic nanoparticles for hyperthermia applications.

## 1. Introduction

Hippocrates stated, “Those diseases which medicines do not cure, iron cures; those which iron cannot cure, fire cures.” Direct heating of a deep-seated tumor with an external flame is impractical, yet a familiar analogy suggests an alternative approach. A frying pan on an induction cooker heats rapidly; however, placing one's hand on the cooker instead does not cause it to become hot, implying that selective internal heating may be possible if a miniature pan can be delivered to the tumor site as an energy absorber from an AC magnetic field. Achieving this requires a carrier smaller than 100 nm to enable transport through the bloodstream, which motivates the use of nanoparticles as the “pan.” At this

scale, conventional induction currents responsible for heating macroscopic metal pans do not arise. Instead, magnetic materials that dissipate energy through hysteresis loss under alternating magnetic fields, such as iron and iron oxides, are suitable candidates. Consequently, the hyperthermic response of magnetic nanoparticles has been widely investigated as a tumor-selective therapy, commonly referred to as magnetic fluid hyperthermia or magnetic nanoparticle hyperthermia [1–5].

Despite its promise, this technique faces significant barriers to clinical translation. The injectable dose of magnetic nanoparticles is limited, and the resulting heat generation is often insufficient for effective tumor ablation. Cellular damage typically begins at 42–43 °C [1–3], yet achieving this temperature uniformly across the target region remains

\* Corresponding author.

E-mail address: [MAMIYA.Hiroaki@nims.go.jp](mailto:MAMIYA.Hiroaki@nims.go.jp) (H. Mamiya).

<https://doi.org/10.1016/j.mtnano.2026.100869>

Received 9 April 2026; Received in revised form 3 June 2026; Accepted 16 June 2026

Available online 17 June 2026

2588-8420/© 2026 The Authors. Published by Elsevier Ltd. This is an open access article under the CC BY license (<http://creativecommons.org/licenses/by/4.0/>).

difficult. Analytical calculations [5,6] and numerical simulations based on human body models [7] estimate that approximately  $0.6 \text{ W/cm}^3$  of heating power is required to raise the temperature of a 1 cm tumor by  $6^\circ\text{C}$ . For comparison, an induction heating (IH) cooker delivers 2–3 kW to a frying pan weighing about 1 kg, corresponding to 2–3 W/g. If the heating power of magnetic nanoparticles were equivalent to that of such a frying pan, achieving  $0.6 \text{ W/cm}^3$  would require nanoparticle density- $\epsilon$  of approximately 0.2 g per cubic centimeter of tumor tissue, which is not feasible. In practice, even with advanced drug delivery methods, only  $\epsilon = 2\text{--}3 \text{ mg/cm}^3$  of iron oxide-based nanoparticles can be loaded into tumor tissue in animal studies [8,9]. Under these constraints, a heating power of 200–300 W/g is required to achieve therapeutic effects, roughly two orders of magnitude higher than that of induction cookers. As a result, research on magnetic nanoparticles for hyperthermia has primarily focused on maximizing heating power.

A wide range of nanoparticle systems has been synthesized to enhance heat generation, and their performance is commonly evaluated using the specific absorption rate of the nanoparticles ( $\text{SAR}_{\text{nano}}$ ), also referred to as specific loss power. Fig. 1(a) summarizes  $\text{SAR}_{\text{nano}}$  values reported for 100 representative nanoparticle systems [5,10–50], [51–58]. Sustained research efforts have yielded numerous nanoparticles with  $\text{SAR}_{\text{nano}}$  values exceeding 200 W/g, which are generally considered sufficient for hyperthermia applications. However, these values have been measured under different magnetic field amplitudes  $H_{\text{AC}}$  and frequencies  $f$  across studies. This variation arises because the resonant frequency of the heating coil in each laboratory's measurement apparatus cannot be easily adjusted. As a result, direct comparison of  $\text{SAR}_{\text{nano}}$  values is difficult. Moreover, experimental conditions dictated by instrument-specific resonance may not correspond to those that maximize the heating performance of the nanoparticles. Evaluating materials under suboptimal conditions or using unsuitable performance metrics hinders material development.

Three representative sample types are selected for analysis; the rationale for this selection is outlined in the following discussion. When ferromagnetic materials such as iron and iron oxides are reduced to sizes on the order of several tens of nanometers, the energy required to form domain walls becomes relatively large, resulting in a stable single-domain state [2]. Under these conditions, each nanoparticle behaves as if it has a single magnetic moment  $\mu$  of magnitude  $\mu = M_s V$  where  $M_s$  is the spontaneous magnetization and  $V$  is the particle volume. Since the magnetic anisotropy energy  $E_a$  rises the orientation energy of  $\mu$  along magnetic hard planes, reversal of  $\mu$  necessitates the application of an external magnetic field exceeding a characteristic switching field  $H_{\text{sw}}$ . As  $E_a$  decreases in proportion to  $V$ , nanoparticles in the 20–30 nm range—commonly used for magnetic hyperthermia—display frequent thermally activated reversals of  $\mu$ , known as Néel relaxation [2].

Previous studies have shown that nanoparticles become immobilized after accumulating in tumors and being internalized by cancer cells [59–62]. Given that the maximum achievable intratumoral concentration  $\epsilon$  is approximately  $3 \text{ mg/cm}^3$ , the average interparticle spacing,  $r$ , corresponds to roughly five particle diameters. If this spacing is preserved as a result of ideal single-particle endocytosis, dipolar interactions of magnitude  $\mu_0 \mu^2 / r^3$  are negligible, where  $\mu_0$  is the vacuum permeability. Consequently, the heating behavior can be reasonably described using a simplified model that includes only thermal Néel relaxation and magnetic field-driven moment reversal for isolated particles, as considered above. To represent this idealized scenario, a model sample was prepared consisting of iron oxide nanoparticles with a core diameter of 17.4 nm (denoted SN17), encapsulated within a thick, nonmagnetic silica shell [63–66]. The coating ensured an interparticle spacing of approximately 4.5 times the core diameter (Fig. 2(d)).

In therapeutic applications, magnetic nanoparticles are administered as magnetic fluids. Within the bloodstream or interstitial fluid, the particles undergo translational and rotational motion, and larger

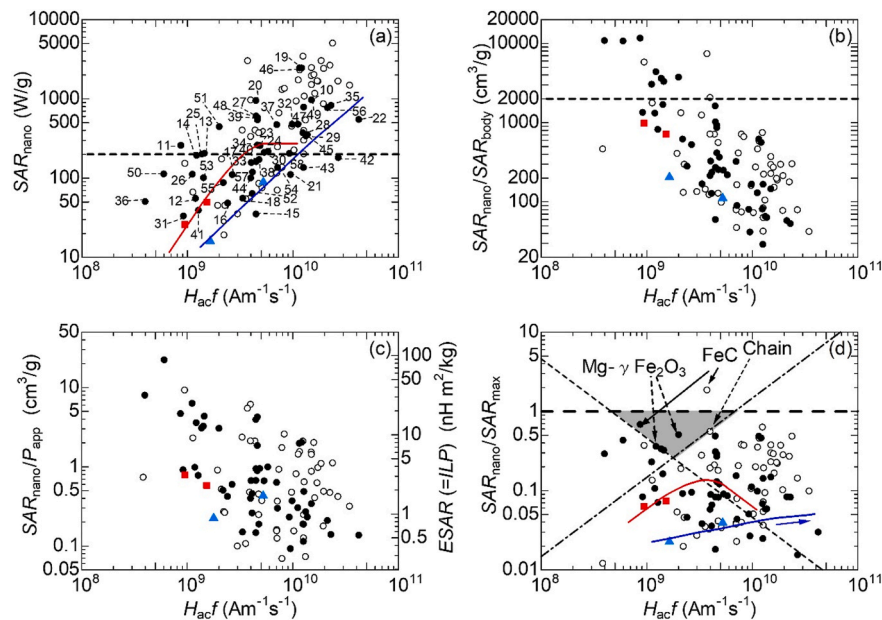


**Fig. 1.** Representative results for 100 magnetic nanoparticle samples irradiated with an alternating magnetic field  $H_{\text{AC}} \sin(2\pi f t)$ , compiled from Ref. [5] ( $\circ$ ), Refs. [10–57] ( $\bullet$ ), and the present study ( $\blacktriangle$  and  $\blacksquare$ ). The data is plotted as a function of the irradiation conditions  $H_{\text{AC}} f$ . (a) Specific absorption rate per unit nanoparticle mass ( $\text{SAR}_{\text{nano}}$ ). Reference numbers correspond to individual data points. The dashed line shows the 200 W/g threshold (see text). The solid blue and red curves show the irradiation-condition dependence estimated using the method developed in this work. (b) Heating selectivity ratio ( $\text{SAR}_{\text{nano}} / \text{SAR}_{\text{body}}$ ), where we use a  $\text{SAR}_{\text{body}}$  value of  $3 \times 10^{-20} (H_{\text{AC}} f)^2$  (units:  $\text{W/cm}^3$ ). The dashed line indicates the 2000-fold threshold described in the text. (c) Specific power factor ( $\text{SAR}_{\text{nano}} / P_{\text{app}}$ ), where  $P_{\text{app}}$  is the apparent power per unit volume. The right-hand axis is labeled according to the relation  $\text{ESAR} = \pi \mu_0 \text{SAR}_{\text{nano}} / P_{\text{app}}$ . (d) Heating efficiency index, defined as the ratio of the observed  $\text{SAR}_{\text{nano}}$  to its theoretical upper limit. The dashed and dash-dotted lines correspond to the 200 W/g line in (a) and the 2000-fold line in (b), respectively. The gray triangular area enclosed by these lines is the practical target. In panels (a)–(d), the data is displayed on a logarithmic scale covering a range of three orders of magnitude. Therefore, when plotting  $\text{SAR}_{\text{nano}}$  values, we did not consider whether the mass of surface modification layers was included in the denominator, and used the values reported in the original references as they were.

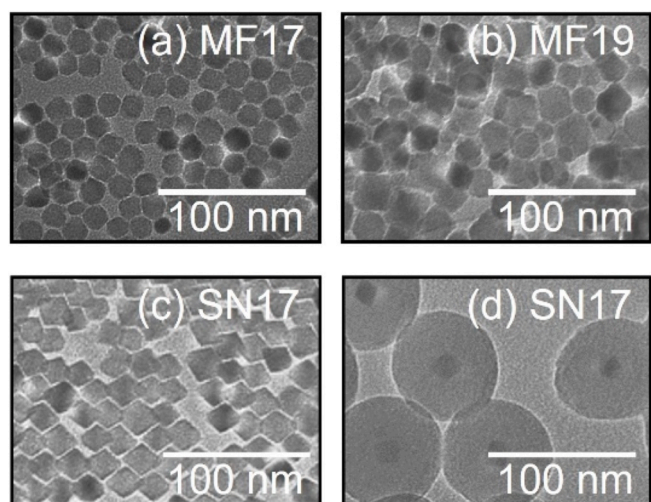


**Fig. 2.** TEM micrographs of magnetic nanoparticles in (a) MF17, (b) MF19, and (c) SN17. (d) TEM micrograph of SN17 after silica coating.

nanoparticles can gradually aggregate due to magnetic attractions at their closest approach, ultimately leading to precipitation [67–69]. The dispersion stability threshold for iron oxide nanoparticles has been reported to lie near 16–17 nm, assuming a surface layer of 1–2 nm [70,71]. Nanoparticles significantly smaller than this threshold have been widely used in industrial magnetic fluids, where long-term stability over product lifetimes of approximately 10 years is required. In contrast, hyperthermia applications require stability only during the short interval between administration and tumor accumulation. After reaching the tumor, partial aggregation into chain-like structures due to dipolar interactions can enhance heating efficiency [72–74]. Therefore, nanoparticles larger than the stability threshold also remain viable candidates as nano thermal seeds.

Based on these considerations, we prepared a magnetic fluid (MF17) containing iron oxide nanoparticles with a particle size of 16.8 nm (slightly smaller than the critical threshold), to model particles capable of undergoing Brownian motion in the interstitial fluid environment. Since the viscosity of blood and interstitial fluid varies greatly depending on its anatomical location and physiological state, low-viscosity kerosene—comparable to plasma viscosity—was selected as the solvent to provide a clear contrast with the immobilized SN17 powder.

On the other hand, various forms can be considered for aggregated nanoparticles whose magnetic response is influenced by dipole–dipole interactions. These include not only chains formed spontaneously through anisotropic magnetic attraction but also clusters formed spontaneously via isotropic van der Waals forces, as well as nanoparticles that are densely packed within endosomes following co-endocytosis. However, this study focuses mainly on the behavior of clusters formed through dipolar interactions. To this end, we prepared a magnetic fluid (MF19) containing iron oxide nanoparticles with a particle size of 19.2 nm, which is slightly larger than the critical threshold.

Based on the above discussion, the primary objective of this study is to identify the key considerations in comparing the hyperthermic effects of magnetic nanoparticles and to propose appropriate performance indicators and screening strategies. To achieve this, representative nanoparticle systems, specifically designed to model sparsely immobilized, dispersed, and aggregated states relevant to magnetic hyperthermia, are used to evaluate the proposed performance indicator and screening methods.

## 2. Experimental

**Preparation of magnetic fluids.** Iron oxide nanoparticle samples MF17 and MF19 were synthesized by dissolving 8 and 9 mmol of tris

(acetylacetonate) iron(III) ( $\text{Fe}(\text{acac})_3$ ), respectively, in a mixture containing equimolar oleic acid (40 mmol) and oleylamine (40 mmol) under continuous stirring at room temperature. Here, oleic acid was used to stabilize the iron complex [75], while oleylamine acted as a reducing agent [76]. The solution was then heated to 393 K and maintained for 1 h under a  $\text{N}_2$  atmosphere, followed by heating to 553 K for 2 h. The resulting nanoparticles were repeatedly washed with toluene to remove excess surfactants. The dried nanoparticles were characterized using transmission electron microscopy (TEM), X-ray diffraction (XRD), X-ray absorption near-edge structure (XANES) spectroscopy, and Mössbauer spectroscopy. Representative micrographs are shown in Fig. 1(a) and (b), and the size distributions are provided in Fig. S1 of the Supplementary Information. The mean particle diameters ( $d_m$ ) were 16.8 nm for MF17 and 19.2 nm for MF19. Analysis of the XRD patterns, XANES spectra, and Mössbauer data (Supplementary Information) indicated that the nanoparticles consist of spinel-type iron oxide, with iron predominantly in the trivalent state. Magnetic fluids MF17 and MF19 were prepared by dispersing the surfactant-coated nanoparticles in kerosene at concentrations of 10 and 7 mg/mL, respectively. For MF17, the dispersion stability remained unchanged even after one year, whereas for MF19, sedimentation was observed within a few days after dispersion. This difference is consistent with the particle size threshold for dispersion instability previously reported [70,71]. The magnetic behavior after sedimentation remained stable and generally reproducible in MF19. Although it is still unclear whether the nanoparticles in MF19 can pass through the blood vessel wall before aggregation occurs, their behavior differs substantially from that of well-dispersed systems such as MF17. Therefore, in this study, we included MF19 as a representative example of aggregated nanoparticles.

**Preparation of silica coated nanoparticle powder.** Silica-coated iron oxide nanoparticles (SN17) were synthesized as follows. First, 8 mmol of  $\text{Fe}(\text{acac})_3$  was dissolved in an equimolar mixture of oleic acid (49 mmol) and oleylamine (49 mmol). Here, oleic acid was used to stabilize the iron complex [1], while oleylamine acted as a reducing agent [2]. The solution was reacted at 393 K for 1 h under a  $\text{N}_2$  atmosphere, followed by heating to 590 K and maintaining this temperature for 2 h to form the iron oxide nanoparticle cores. Silica coating was then carried out using a microemulsion method. A surfactant phase was prepared by dispersing 4 g of polyoxyethylene (5) nonylphenylether in 90 mL of cyclohexane under sonication. Subsequently, 12 mg of the washed nanoparticles was added under continuous stirring, followed by the dropwise addition of 3.2 mL of 25% ammonium hydroxide and 5.6 mL of tetraethyl orthosilicate (TEOS). Electron micrographs of the nanoparticles before and after silica coating are presented in Fig. 1(c) and (d). The octahedral iron oxide cores encapsulated within a thick, nonmagnetic silica shell are clearly visible. The distribution of effective diameters, defined as the diameter of a circle with the same cross-sectional area as the iron oxide core, is shown in Fig. S1 (Supplementary Information). The mean effective diameter was 17.4 nm, and the silica shell thickness was approximately 30 nm. Analysis of the XRD patterns, and XANES spectra (Supplementary Information) indicated that the particles consist of spinel-type iron oxide, with iron predominantly in the trivalent oxidation state.

**Magnetic and hyperthermic measurements.** The static magnetization  $M_{\text{DC}}$  of MF17 and MF19 was measured using vacuum-tight liquid cells and the extraction method in a PPMS magnetometer (Quantum Design) under steady magnetic fields up to 125 kA/m.  $M_{\text{DC}}$  of SN17 was measured using a SQUID in an MPMS3 magnetometer (Quantum Design) over the same field range. Isothermal remanent magnetization (IRM) was generated by applying a static field  $H$  for 1 min after zero-field cooling from the thermally demagnetized state, followed by switching off the field. The subsequent thermal decay of IRM was recorded as a function of temperature during heating.

Magnetic hyperthermia measurements for MF17 and MF19 were conducted using a MagneTherm™ system (Nanotherics). Samples were thoroughly mixed immediately before exposure to the AC magnetic



field. The excitation frequency ( $f$ ), monitored using a frequency counter, ranged from 110 to 990 kHz. The field amplitude  $H_{AC}$ , determined from the induced voltage of a pickup coil, did not exceed 14 kA/m. Sample temperatures were measured using an optical fiber thermometer, and the heating power was calculated from the initial rate of temperature increase.

Hyperthermia experiments were not performed for the silica-coated powder SN17 because the heat capacity and thermal conductivity of the silica shell cannot be reliably determined. Instead, the hysteresis loss was inferred from the area of the dynamic BH loop. AC magnetic fields were generated using an LCR series resonant circuit with an air-core solenoid coil driven by a 1 kW RF power supply (Thamway, T162-6013AHE). The maximum magnetic field amplitude  $H_{AC}$  was 63.7 kA/m when the excitation frequency  $f$  was 58 kHz. A figure-eight coil placed inside the solenoid detected the sample-induced electromotive force. The signals, recorded on a digital oscilloscope (Teledyne LeCroy HDO4034A), were integrated and converted into the time-dependent magnetization  $M_{AC}$ .

### 3. Specific absorption rate and figure of merit

First, the heating characteristics of MF17 and MF19 were evaluated using the specific absorption rate ( $SAR_{nano}$ ) per unit mass of the magnetic nanoparticles. Fig. 3(a) shows the  $SAR_{nano}$  of MF17 measured across various frequencies  $f$  and magnetic-field amplitudes  $H_{AC}$ . The values increased with frequency, reaching 89 W/g at 523 kHz and 10 kA/m. For comparison with previously reported data, the  $SAR_{nano}$  values (10 kA/m) for MF17 at two different frequencies have been added to Fig. 1(a). On the other hand, MF19 exhibited substantial heating at high  $H_{AC}$ , achieving 49 W/g at 110 kHz and 14 kA/m, as shown in Fig. 3(b). Its  $SAR_{nano}$  values at 110 kHz for two field amplitudes are also added in Fig. 1(a). As shown in Fig. 1(a), the absolute  $SAR_{nano}$  values for both samples are significantly lower than those reported previously and fall well below the threshold of 200 W/g. These observations raise questions about the heat generation performances of MF17 and MF19, if they were inherently inferior to that of existing nanoparticles, and if they were unlikely to reach the threshold for practical application. To address these questions, the trends observed for MF17 to the upper bounds of previously employed experimental conditions were extrapolated; the

basis for this extrapolation is discussed later. The results indicate that  $SAR_{nano}$  exceeds 200 W/g at higher frequencies. Furthermore, at the highest  $H_{AC}f$  values, the expected  $SAR_{nano}$  is approximately 1000 W/g, comparable to previously reported values shown in Fig. 1(a).

The above-mentioned example highlights two key issues when comparing heating performance across studies: (i) measurements are not conducted under uniform irradiation conditions, and (ii) experimental conditions are often not optimized for the specific nanoparticles. Therefore, we must examine whether a more appropriate performance metric can enable meaningful comparison of heating characteristics across nanoparticles evaluated under different experimental conditions. As seen in Fig. 1(a), previously reported  $SAR_{nano}$  generally increases with the product  $H_{AC}f$ . We shall consider the validity of  $SAR_{nano}$  as a comparative metric by investigating the origin of this behavior.

For magnetic nanoparticles, the time-averaged  $SAR_{nano}$  generated by an AC magnetic field  $\mathbf{H} = (0, 0, H_{AC}\sin(2\pi ft))$  is defined as:

$$SAR_{nano} \sim (\rho V)^{-1} \mu_0 f \int \oint \mathbf{H} \cdot d\mathbf{M} dV, \quad (1)$$

irrespective of whether energy dissipation occurs through hydrodynamic viscosity or magnetic friction, where  $\rho$ ,  $V$ , and  $\mathbf{M}$  are the density, volume, and magnetization, of the nanoparticle, respectively (See the Supplementary Information for the derivation.) In the case of single-domain particles, the component of  $\int \mathbf{M} dV$  parallel to  $\mathbf{H}$  is defined as  $\mu \cos \theta = M_s V \cos \theta$ , where  $\theta$  represents the angle between the magnetic moment  $\mu$  and the external field  $\mathbf{H}$ . Substituting this expression in Eq (1), we get:

$$SAR_{nano} = \rho^{-1} \mu_0 M_s (H_{AC} f) \oint \sin(2\pi ft) d(\cos \theta). \quad (2)$$

Based on this expression,  $SAR_{nano}$  is obtained as the product of the irradiation-dependent factor  $H_{AC}f$ , and the term  $\oint \sin(2\pi ft) d(\cos \theta)$ , which reflects the dynamic reorientation of  $\mu$ . Therefore, even if two samples exhibit the same rotational or reversal motion of  $\mu$  driven by the variation in  $H_{AC}\sin(2\pi ft)$ , the measured  $SAR_{nano}$  will differ in proportion to  $H_{AC}f$ . This dependence explains the general trend in Fig. 1(a), where  $SAR_{nano}$  systematically increases with  $H_{AC}f$ . In other words, large  $SAR_{nano}$  values observed in the upper-right region of Fig. 1(a) do not necessarily indicate superior intrinsic reorientation mechanisms with

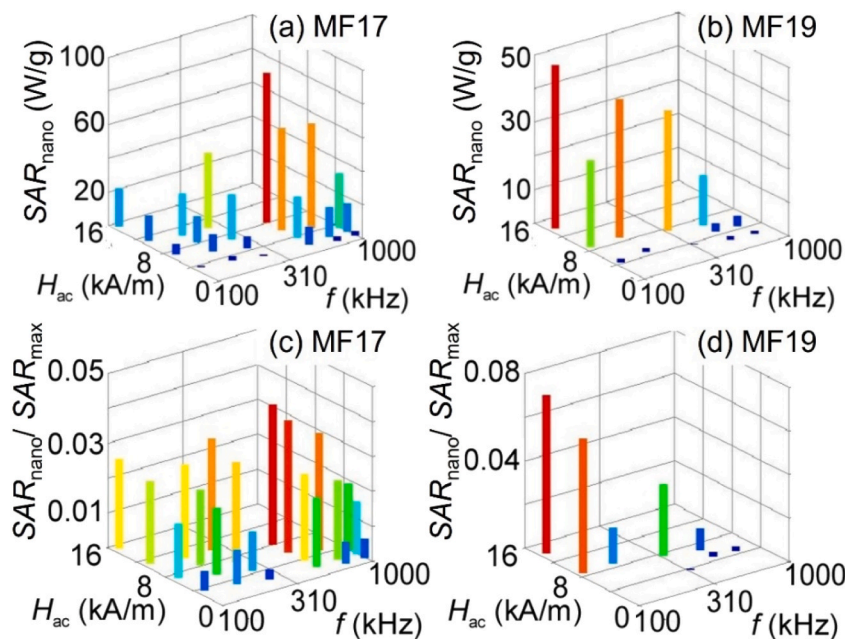


Fig. 3. Specific absorption rate  $SAR_{nano}$  (a, b) and heating efficiency index  $SAR_{nano}/SAR_{max}$  (c, d) of iron oxide nanoparticles in MF17 (a, c) and MF19 (b, d), measured at magnetic field amplitudes  $H_{AC}$  and frequencies  $f$ .

high heat dissipation; they may simply reflect measurement conditions with exceptionally high  $H_{ac}f$ .

Consequently, reliance on  $SAR_{nano}$  as the sole figure of merit for nanomaterial development requires careful reconsideration, because it may cause optimization efforts to shift from improving the intrinsic dynamic response of nanoparticles to merely increasing the field amplitude and frequency. That being said, higher  $H_{ac}$  and  $f$  would be unproblematic if they posed no risks to the human body and imposed no additional burden on the therapeutic systems and clinical conditions that impose strict constraints.

A primary concern is with using  $SAR_{nano}$  as the sole figure of merit for nanomaterial development is unintended heating of healthy tissue. Taguchi et al. [77] estimated that when Japanese adult biologically male models were exposed to a uniform high-frequency magnetic field ( $H_{ac} = 1$  A/m,  $f = 10$  MHz), heat generation of up to  $SAR_{body} = 20$   $\mu$ W/g occurred depending on the region of the body. This corresponds to a  $SAR_{body}$  value of  $2 \times 10^{-19}$  ( $H_{ac}f$ )<sup>2</sup> (units: W/cm<sup>3</sup>). Shoshiashvili et al. [7] demonstrated that the heat generation in healthy tissue can be reduced by using an optimized coil design that spatially concentrates the magnetic field. Their calculation shows that the coefficient of ( $H_{ac}f$ )<sup>2</sup> can be reduced to as low as  $3 \times 10^{-20}$ . Regulatory guidelines for electromagnetic exposure generally restrict the magnitude of  $H_{ac}f$  because exposure duration cannot be controlled in daily-life environments [78].

Similar constraints are applied in therapeutic contexts to ensure patient safety. A well-known example is the Atkinson–Brezovich limit, which constrains  $H_{ac}f < 4.85 \times 10^8$  Am<sup>-1</sup>s<sup>-1</sup> [79]. In actual hyperthermia clinical trials, irradiation conditions of  $H_{ac}f \sim 1.8 \times 10^9$  Am<sup>-1</sup>s<sup>-1</sup> [80] or  $H_{ac}f \sim 2.3 \times 10^9$  Am<sup>-1</sup>s<sup>-1</sup> [81] are sometimes employed after weighing the risks and benefits. In clinical settings, however, intermittent irradiation is feasible; therefore, it would be more appropriate to evaluate side effects using the heating selectivity ratio,  $SAR_{nano}/SAR_{body}$ . Fig. 1(b) presents previously reported data re-expressed using this ratio, where we used the above-mentioned values  $3 \times 10^{-20}$  ( $H_{ac}f$ )<sup>2</sup> for  $SAR_{body}$ . (It should be noted that the coefficient of the ( $H_{ac}f$ )<sup>2</sup> dependence of  $SAR_{body}$  varies depending on the model or device used; therefore, as advancements are made in the field of hyperthermia apparatus, the vertical axis of this logarithmic graph will need to be updated accordingly.) In any case, regardless of whether the revision of the coefficient causes a vertical shift of the entire plot in this logarithmic graph, it is evident that lower selectivity ratios occur at higher  $H_{ac}f$  values, indicating that nanoparticles exhibiting high  $SAR_{nano}$  under strong irradiation are not necessarily optimal for minimizing off-target heating. However, it is not straightforward to define a universal threshold for how much reduction in this selectivity ratio can be tolerated. To address this issue, we assume that when the temperature of tumor tissue rises by 6°C, the temperature increase in normal tissue must be less than 1°C. Under the rough assumption that specific heat and thermal diffusivity are the same, this corresponds to the requirement that the heat generated in the tumor  $\epsilon SAR_{nano}$  must be at least six times greater than in normal tissue  $SAR_{body}$ . Taking the previously mentioned  $\epsilon$  value of 3 mg/cm<sup>3</sup> in the tumor, the acceptable ratio of  $SAR_{nano}$  to  $SAR_{body}$  would be 2000-fold. As shown in Fig. 1(b), when the  $H_{ac}f$  value is high, the reported ratios of  $SAR_{nano}/SAR_{body}$  are generally low and far below this threshold.

On the other hand, several nanoparticles achieve selectivity ratios exceeding this threshold under conditions where  $H_{ac}f$  is small. Does this imply that these particles possess an intrinsic reorientation mechanism that results in minimal side effects? To clarify this question, the heating selectivity ratio is reformulated using Eq. (3):

$$\frac{SAR_{nano}}{SAR_{body}} = \frac{\mu_0 M_s}{3 \times 10^{-20} \rho H_{ac} f} \oint \sin(2\pi f t) d(\cos \theta). \quad (3)$$

From this equation, it is evident that the heating selectivity ratio includes a coefficient that is inversely proportional to  $H_{ac}f$ , independently of the term  $\oint \sin(2\pi f t) d(\cos \theta)$ . In other words, even if two

samples exhibit the same rotational or reversal motion of  $\mu$  driven by the variation in  $H_{ac} \sin(2\pi f t)$ , the measured  $SAR_{nano}/SAR_{body}$  will differ in inverse proportion to  $H_{ac}f$ . Therefore, when the reduction of side effects is to be achieved through improvement of the dynamic reorientation mechanism of  $\mu$ , it may not be appropriate to compare the performance of the synthesized nanoparticle solely based on the selective heating ratio.

Next, let us consider the constraints related to clinical instrumentation. In therapeutic systems, large air-core coils are employed to irradiate either the entire trunk or localized regions of the body, with typical coil volumes  $v_{coil}$  of  $4 \times 10^4$  cm<sup>3</sup> [82] and  $10^3$  cm<sup>3</sup> [83,84] respectively. In comparison, the tumor volume  $v_{tumor}$  is extremely small, and the volume occupied by nanoparticles within the tumor is even smaller. For example, in a tumor with a diameter of 1 cm ( $v_{tumor} \sim 0.5$  cm<sup>3</sup>), the amount of magnetic nanoparticles, assuming  $\epsilon = 3$  mg/cm<sup>3</sup>, is only 1.5 mg. Under such conditions, most of the electrical power supplied to the coil is reactive, and the apparent power can be approximated by the reactive power:  $v_{coil} P_{app} = v_{coil} (\pi f \mu_0 H_{ac}^2)$ . Therefore, minimizing  $v_{coil} P_{app}$  while maximizing heat generation  $\epsilon v_{tumor} SAR_{nano}$  is essential for reducing the required power supply rating. The ratio  $\epsilon v_{tumor} SAR_{nano} / v_{coil} P_{app}$  corresponds to the power factor of the instrumentation. For this reason, the ratio of  $SAR_{nano}/P_{app}$ , excluding treatment-related factors, is referred to here as the specific power factor. Therefore, nanoparticles with a specific power factor are desirable in terms of device load. Except for the constant term  $\pi \mu_0$ , the specific power factor is equivalent to the widely used effective specific absorption rate (ESAR) [85], also called intrinsic loss power (ILP) [86]. ESAR (i.e., ILP) has conventionally been treated as an indicator of relaxation losses within the linear response regime  $\mu_0 \mu H_{ac} \ll k_B T$ . However, for 17 nm iron oxide nanoparticles with a typical  $M_s$  of 450 kA/m [87], the Zeeman energy  $\mu_0 \mu H_{ac}$  already exceeds the thermal energy at room temperature when  $H_{ac} > 3$  kA/m. Consequently, ESAR (i.e., ILP) values derived from the current measurements at  $H_{ac} > 3$  kA/m do not accurately characterize the performance of relaxation losses. Nevertheless, as mentioned above, ESAR (i.e., ILP), which is identical to the specific power factor, remains a meaningful figure of merit because it captures the balance between heating efficiency and device load.

Fig. 1(c) presents the specific power factor,  $SAR_{nano}/P_{app}$  and the ESAR (i.e., ILP), which is  $SAR_{nano}/P_{app}$  multiplied by  $\pi \mu_0$ , for the 100 datasets analyzed in this work. The results show that higher values are consistently obtained at lower  $H_{ac}f$ . To clarify the origin of this trend, the specific power factor was reformulated using Eq. (3):

$$\frac{SAR_{nano}}{P_{app}} = \frac{ESAR}{\pi \mu_0} = \frac{ILP}{\pi \mu_0} = \frac{M_s}{2\pi \rho H_{ac}} \oint \sin(2\pi f t) d(\cos \theta), \quad (4)$$

Based on this expression, the specific power factor increases as  $H_{ac}$  decreases, regardless of the term  $\oint \sin(2\pi f t) d(\cos \theta)$ . In other words, higher  $SAR_{nano}/P_{app}$  ratios observed in the upper-left region of Fig. 1(c) do not necessarily indicate superior intrinsic reorientation mechanisms of  $\mu$  with high active power.

The preceding discussion shows that,  $SAR_{nano}$  intrinsically increases with higher  $H_{ac}$  and  $f$ . In contrast, indicators related to safety and device burden, namely the heating selectivity ratio  $SAR_{nano}/SAR_{body}$  and the specific power factor  $SAR_{nano}/P_{app}$ , tend to improve as  $H_{ac}$  and  $f$  are reduced (and only  $H_{ac}$  in the latter case), irrespective of the magnetic response of  $\mu$ . Needless to say, if all the practical constraints described above could be satisfied solely by optimizing  $H_{ac}$  and  $f$ , there would be no difficulties. Nonetheless, the directions of changing  $H_{ac}$  and  $f$  for improving heating power and ensuring safety are fundamentally opposed. Therefore, it is challenging to simultaneously achieve therapeutic effects via tumor heating and minimize side effects associated with the heating of normal tissue merely by adjusting the magnetic field irradiation conditions.

Reconciling therapeutic efficacy with the minimization of side effects would require materials with enhanced intrinsic heat-generation

mechanisms, rather than nanoparticles that appear effective only under favorable irradiation conditions. To address this, we should draw attention to the term representing the dynamic reorientation mechanisms of  $\mu$ ,  $\oint \sin(2\pi ft)d(\cos \theta)$  without explicitly including the irradiation conditions. This term reaches a maximum value of 4 when  $\theta$  changes abruptly from  $-\pi$  to  $+\pi$  at  $t = 1/4f$  and reverses at  $t = 3/4f$ . In other words,  $SAR_{\text{nano}}$  can be maximized at  $SAR_{\text{max}} = \rho^{-1} 4\mu_0 M_s (H_{\text{ac}} f)$  whenever ideal reorientation occurs, irrespective of factors such as the presence or absence of interparticle interactions, or whether energy dissipation occurs through hydrodynamic viscosity or magnetic friction. Accordingly, we propose a heating efficiency index  $\frac{SAR_{\text{nano}}}{SAR_{\text{max}}} = \frac{1}{4} \oint \sin(2\pi ft)d(\cos \theta)$  that reflects the intrinsic heat-generation mechanisms of the synthesized nanoparticles. This metric fundamentally measures how closely the ideal rotation or reversal motion of  $\mu$  is realized under given irradiation conditions, thereby providing guidance for the development of magnetic nanoparticles. It should be noted that, for any magnetic response mechanism, the range of irradiation conditions under which ideal or near-ideal rotational or reversal motion is exhibited is limited, and it is not self-evident whether the measurement conditions used in experiments actually correspond to this optimal range. This highlights the need for evaluation across the broadest possible range of irradiation conditions; however, further discussion on this will be undertaken in the next section “Screening using blocking temperature and switching field distribution”. Here, irrespective of whether the optimal irradiation conditions were used, we first examine the distribution of previously reported values using this proposed metric.

Fig. 1(d) presents the heating efficiency index  $SAR_{\text{nano}}/SAR_{\text{max}}$  calculated from previously reported data, where  $M_s$  and  $\rho$  are uniformly set to typical values of 450 kA/m and 5200 kg/m<sup>3</sup> for bulk iron oxide [87] for simplifying the estimation. (At this stage, since the comparison is limited to a logarithmic scale, this simplification does not have any notable effect on the results, except for the case of metallic cores, which will be discussed later.) When the criteria discussed in Fig. 1(a) and (b) are superimposed as dashed and dotted lines, respectively, the region satisfying both conditions corresponds to the central triangular zone highlighted in gray. Magnetic nanoparticles intended for hyperthermia must therefore achieve  $SAR_{\text{nano}}/SAR_{\text{max}}$  values within this region. A small number of reported nanoparticles already meet these requirements. The first group, indicated by solid arrows [11,88], consists of iron-based metallic nanoparticles. Because their  $M_s$  values are significantly higher than those of iron oxide, they can generate a large amount of heat. (Since the current plotting uniformly uses the  $M_s$  value of bulk iron oxide (450 kA/m) for simplifying the calculation, the efficiency index appears to exceed the theoretical upper limit, although this is merely an apparent effect). However, the chemical instability of highly reactive metallic nanoparticles with large surface areas remains a concern for biomedical applications. The second group comprises bacterial magnetosomes, indicated by dashed arrows [73]. These iron oxide nanoparticles are known to form chain-like clusters, and the collective magnetic response of  $\mu$ , along with the resulting effective magnetic anisotropy arising from interparticle interactions, has been proposed as the origin of their high  $SAR_{\text{nano}}/SAR_{\text{max}}$  values. However, clustering prior to reaching the tumor interstitial fluid can hinder vascular wall penetration, necessitating careful control of aggregation in hyperthermia applications involving intravenous administration. The third group includes Mg-doped maghemite nanoparticles [14,51]. These oxide nanoparticles exhibit exceptionally high heating performance despite moderate  $M_s$  values of 330–350 kA/m. Although the underlying mechanisms require further investigation, these results suggest that both criteria can be satisfied by optimizing the dynamic magnetic response of isolated, stable iron oxide nanoparticles, without relying on metallic iron or aggregates. The objective of this study is to examine indicators for the appropriate comparison of data obtained under different irradiation conditions. Accordingly, the 100 data points considered here do not represent the entirety of reported results. Setting aside the

interpretation of individual cases,  $SAR_{\text{nano}}/SAR_{\text{max}}$  provides insight into improving the efficiency of heat generation during reorientation of  $\mu$ . The discrepancy between the theoretical maximum and the experimental values in Fig. 1(d) indicates the extent of potential for performance improvement in nanoparticle development by controlling the reorientation mechanisms of  $\mu$ .

It is extremely challenging to achieve complete and instantaneous reorientation of  $\mu$  at the optimal AC field phase in actual polydisperse nanoparticles within tumors. Therefore, rather than relying on serendipitous improvements, promoting material development aimed at approximating this ideal rotational or inversion motion of  $\mu$  as closely as possible will significantly accelerate the creation of high-performance nanoparticles. In this context, it is desirable for development to proceed along a vector connecting the current state to the target region defined by the practical requirements (represented by the triangular area in Fig. 1(d)). As discussed in last section, the proposed metric,  $SAR_{\text{nano}}/SAR_{\text{max}}$ , reflects only the contribution of the dynamic response of  $\mu$  and therefore serves as a convenient measure for comparing and improving intrinsic heating mechanisms. In contrast, conventional metrics, namely  $SAR_{\text{nano}}$ ,  $SAR_{\text{nano}}/SAR_{\text{body}}$  and  $SAR_{\text{nano}}/P_{\text{app}}$ , change with irradiation conditions even when the underlying magnetic dynamics remain unchanged as summarized in Table 1. Consequently, these conventional metrics alone are not sufficient to fully evaluate the intrinsic heating performance of magnetic nanoparticles.

We examine the performance of the two magnetic fluids synthesized in this study using the metric  $SAR_{\text{nano}}/SAR_{\text{max}}$ . As shown in Fig. 2(c), the ratio for MF17 increases with frequency, rising from 0.022 at 174 kHz to 0.039 at 523 kHz under a field amplitude of 10 kA/m. In contrast, Fig. 2(d) shows that MF19 exhibits higher  $SAR_{\text{nano}}/SAR_{\text{max}}$  at larger  $H_{\text{ac}}$ , increasing from 0.063 at 8.7 kA/m to 0.073 at 14 kA/m at 110 kHz. Representative values are included in Fig. 1(d). These results indicate that the heating efficiencies of MF17 and MF19 under the present irradiation conditions are modest compared with previously reported values, suggesting that there is significant room for improvement in the magnetic response mechanism. If candidate materials were screened solely on this basis, these magnetic fluids would currently be considered unsuitable for hyperthermia applications. However, this is a premature conclusion for the reasons explained below.

Within the accessible range of irradiation parameters,  $SAR_{\text{nano}}/SAR_{\text{max}}$  for MF17 improves with increasing  $f$ , whereas that for MF19 improves with increasing field amplitude. This suggests that, for both materials, there remains a possibility that they may exhibit substantially superior performance and fulfill the practical requirements indicated by

**Table 1**  
Summary of performance metrics for magnetic nanoparticle heating.

Metric	Physical Meaning	Irradiation Condition Dependence	Typical Use
Specific Absorption Rate: $SAR_{\text{nano}}$ (W/g)	Heat generated per unit mass of nanoparticles	Directly	Evaluation of heating power
Heating Selectivity Ratio: $\frac{SAR_{\text{nano}}}{SAR_{\text{body}}}$ (cm <sup>3</sup> /g)	Selectivity for tumour vs. normal tissue	Directly	Side effects evaluation
Specific Power Factor: $\frac{SAR_{\text{nano}}}{P_{\text{app}}}$ (cm <sup>3</sup> /g) (= $\pi\mu_0 ILP$ ) (ILP = $\pi\mu_0 ESAR$ )	Heating power per device load	Directly	Device load evaluation
Heating Efficiency index: $\frac{SAR_{\text{nano}}}{SAR_{\text{max}}}$ (Dimensionless)	Heating efficiency compared to theoretical maximum	Nanoparticle-specific	Nanoparticle development



the triangular region under conditions exceeding the limits of the current measurement system. Because the excitation parameters of high-frequency heating devices are constrained by their resonant characteristics, the following section examines whether alternative methods can be used to estimate heating performance over a broader operational range.

Before concluding this section, it should be noted that, in Fig. 1, the values reported in the original literature were used directly for  $SAR_{\text{nano}}$ , without considering whether the denominator included the mass of the surface-modified layer or oxygen during the calculation. At this stage, since the comparison is limited to a logarithmic scale, this rough normalization does not significantly affect the results. More detailed comparisons will be undertaken as part of the future scope of this work. However, to do so, standardizing these factors across studies will be necessary.

#### 4. Screening using blocking temperature and switching field distribution

Evaluation of the magnetic fluids MF17 and MF19 showed that their  $SAR_{\text{nano}}/SAR_{\text{max}}$  values do not exceed previously reported values. However, both samples exhibit an increasing trend in  $SAR_{\text{nano}}/SAR_{\text{max}}$  at the boundary of the current measurement range, suggesting the potential for enhanced performance under optimized irradiation conditions beyond this range. To confirm this possibility, it is necessary to determine whether these trends persist beyond the operational limits of the current instrumentation. As a first step, conventional models describing frequency- and magnetic field-dependent heating losses were revisited and compared with experimental data obtained from a simple reference system: spatially immobilized, magnetically isolated iron oxide nanoparticles (SN17). In this model system, dipolar interactions are effectively suppressed by a thick nonmagnetic shell, as confirmed by first-order reversal curve (FORC) analysis (Supplementary Information).

For frequency-dependent loss (relaxation loss), the standard linear-response model under small-amplitude magnetic fields ( $\mu_0\mu H_{\text{ac}} \ll k_B T$ ) provides the fundamental model:

$$M = \chi' H_{\text{ac}} \sin(2\pi f t) - \chi'' H_{\text{ac}} \cos(2\pi f t) \\ = \frac{\chi_0}{1 + (2\pi f \cdot \tau)^2} H_{\text{ac}} \sin(2\pi f t) - \frac{\chi_0 \cdot 2\pi f \cdot \tau}{1 + (2\pi f \cdot \tau)^2} H_{\text{ac}} \cos(2\pi f t), \quad (5)$$

where  $\chi_0$ ,  $\chi'$ , and  $\chi''$  denote the static susceptibility, in-phase, and out-of-phase component of AC susceptibility, respectively, and  $\tau$  denotes the relaxation time. In the case of immobilized nanoparticles,  $\tau$  corresponds to the Néel relaxation time,  $\tau_N$ :

$$\tau_N = f_0^{-1} \cdot \exp(E_a / k_B T), \quad (6)$$

where  $f_0$  is the attempt frequency typically in the range of  $10^9$  to  $10^{11} \text{ s}^{-1}$ . Substituting Eq. (6) into Eq. (2) shows that the heating efficiency index  $SAR_{\text{nano}}/SAR_{\text{max}}$  reaches its maximum value when the  $\chi''$  peaks. This occurs when  $\tau_N$  is equal to  $(2\pi f)^{-1}$ . Thus, identifying that maximum heating efficiency requires adjusting the measurement frequency to match the actual relaxation time.

Fig. 4(a) presents the frequency dependence of  $\chi''$  for SN17 at  $T = 94 \text{ K}$  under an AC magnetic field with a small amplitude ( $H_{\text{ac}} = 0.8 \text{ kA/m}$ ,  $\mu_0\mu H_{\text{ac}} \ll k_B T$ ). The peak in  $\chi''$  occurs around 0.27 kHz in the absence of a magnetic field, yielding a relaxation time  $\tau_p$  of  $1/(2 \times \pi \times 270) = 0.6 \text{ ms}$ . At first glance, this suggests that the optimal heating frequency at this temperature is 0.27 kHz. However,  $\chi''(f)$  shifts toward higher frequencies under applied bias fields  $H_b$ , demonstrating that the optimal heating frequency varies with small changes in magnetic field conditions. As shown in the inset, the measured variation in  $\tau_p$  with  $H_b$  agrees with the dependence predicted by the conventional model, in which the relaxation time in an applied field is expressed as:

$$\tau_N^{-1} = f_0 \left[ 1 - \left( \frac{H}{H_K} \right)^2 \right] \left[ \left( 1 - \frac{H}{H_K} \right) \exp \left( \frac{-E_a(H=0)}{k_B T} \left( 1 - \frac{H}{H_K} \right)^2 \right) + \left( 1 + \frac{H}{H_K} \right) \exp \left( \frac{-E_a(H=0)}{k_B T} \left( 1 + \frac{H}{H_K} \right)^2 \right) \right] \quad (7)$$

with anisotropy field  $H_K$  [89]. This correspondence indicates that, if both  $E_a(H=0)$  and  $H_K$  are known, heating performance can be estimated over a wide range of irradiation conditions. However, another important feature should be noted: the  $\chi''(f)$  peak measured in zero field is substantially broader than the curve calculated for monodisperse particles with a uniform  $\tau_N$  using Eq. (5). This broadening reflects a distribution of relaxation times, or equivalently of  $E_a(H=0)$ , arising from unavoidable variations in the size and shape of synthesized nanoparticles. A similar distribution also affects  $H_K$ , as discussed later. These observations indicate that accurate prediction of the conditions that maximize the heating efficiency index  $SAR_{\text{nano}}/SAR_{\text{max}}$  requires explicit consideration of the distributions of both  $E_a(H=0)$  and  $H_K$ , rather than relying solely on their mean values.

Next, we consider  $H_{\text{ac}}$  dependent loss due to the magnetization reversal caused by the magnetic field, which is known as the hysteresis loss. In this case, Eq. (2) indicates that  $SAR_{\text{nano}}/SAR_{\text{max}} = \frac{1}{4} \oint \sin(2\pi f t) d(\cos \theta)$  reaches its maximum value on the condition that the largest change in  $\theta$  due to the reversal of  $\mu$  occur when  $H$  reaches maxima  $\pm H_{\text{ac}}$  at  $2\pi f t = \pi/2, 3\pi/2$ . Based on this relationship, it is evident that, to maximize  $SAR_{\text{nano}}/SAR_{\text{max}}$ ,  $H_{\text{ac}}$  must be adjusted to match the dynamical switching field  $H_{\text{SW}}$  of the nanoparticle.

We now examine the switching behavior observed in SN17. Fig. 4(b) shows the magnetization curves at low temperatures. The demagnetization curves in the first quadrant match the theoretical predictions for single-domain particles with randomly-oriented easy axes in the Stoner–Wohlfarth model [5]. The coercivity  $H_c$  at 2 K was measured to be 25 kA/m in the third quadrant.

Does this imply that the optimal  $H_{\text{ac}}$  is 25 kA/m? Notably,  $H_c$  decreases with increasing temperature. These observations indicate that the optimal  $H_{\text{ac}}$  is not 25 kA/m and that the probabilistic reversal induced by thermal fluctuations and the resulting changes in the dynamical switching field must be considered to estimate the optimal  $H_{\text{ac}}$  at finite temperatures.

As shown in the inset, the decrease in  $H_c(T)$  with increasing  $T$  scales as  $T^{0.77}$ . This behavior is consistent with phenomenological relationships reported for randomly oriented particles [90]:

$$H_c(T) \sim H_c(T=0) \cdot \left[ 1 - (T/T_b(t_m, H=0))^{0.77} \right], \quad (8)$$

where  $H_c(T=0)$  is the coercivity at absolute zero and is defined as  $H_c(T=0) = 0.49 H_K$  in the simplest Stoner–Wohlfarth model for randomly oriented nanoparticles.  $T_b(t_m, H=0)$  is the blocking temperature below which  $\mu$  cannot overcome the anisotropy barrier  $E_a(H=0)$  within the measurement time  $t_m$  because the thermal activation is insufficient. Substituting the relation  $\tau_N(T_b) = t_m$  into Eq. (6) shows that  $T_b(t_m, H=0)$  is proportional to  $E_a(H=0)$ , with the proportionality constant given by  $[k_B \ln(t_m \cdot f_0)]^{-1}$ . The agreement between the measured  $H_c(T)$  affected by the probabilistic thermal reversals and the theoretical prediction of Eq. (8) indicates that, if both  $E_a(H=0)$  and  $H_K$  are known, the optimal heating conditions can be estimated over a wide range of irradiation parameters.

However, another behavior in the third quadrant of Fig. 4(b) should be noted. The decrease in magnetization during reversal is considerably more gradual than the dashed curve predicted by the Stoner–Wohlfarth model. This indicates that both the dynamical switching field  $H_{\text{SW}}$  and the underlying anisotropy field  $H_K$  vary from particle to particle. As already discussed,  $E_a(H=0)$  is also broadly distributed. These variations arise from unavoidable heterogeneity in nanoparticle size and shape. Consequently, accurate estimation of the optimal  $H_{\text{ac}}$  requires consideration of the distributions of both  $E_a(H=0)$  and  $H_K$ .

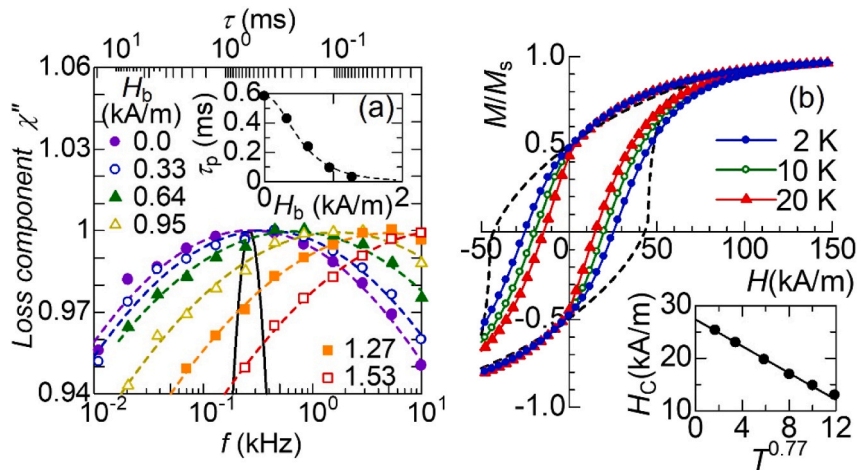


**Fig. 4.** Magnetic properties of SN17. (a) Frequency dependence of the out-of-phase AC susceptibility component  $\chi''$  under various bias fields  $H_b$  normalized to unity. The inset shows the  $H_b$  dependence of the mode relaxation time  $\tau_p$ , calculated from the peak position of  $\chi''$ . (b) Temperature dependence of the magnetization curve. The broken line represents the Stoner–Wohlfarth model. The inset shows the coercive field  $H_c$  as a function of 0.77th power of temperature.

The observational results discussed here demonstrate that the relaxation time for thermally activated magnetization reversal depends on the applied magnetic field. Whereas, the switching field governing field-driven reversal dynamically depends on thermal fluctuations. Moreover, both quantities exhibit significant distributions. Without simultaneously accounting for thermal activation and magnetic anisotropy, namely the distributions of relaxation time (or barrier height) and switching field (or anisotropy field), it is difficult to extrapolate the heating efficiency index beyond the excitation range accessible to conventional heat-generation measurement systems. This raises a key question: can the barrier height and switching-field distributions be

determined concurrently? The following section examines methodological approaches to address this issue.

Conventionally, the  $H_{SW}$  distribution has been estimated using the following property: once magnetization reversal occurs upon the temporary application of a field  $H_r$ , the change remains irreversible after the field is removed. Consequently, the isothermal remanent magnetization (IRM) represents the cumulative magnetization of all nanoparticles with switching fields below  $H_r$ :  $IRM = \sum_{H_{SW} < H_r} \mu$  [91].

Fig. 5(a) presents the minor hysteresis loops of SN17 obtained during temporary application of  $H_r$  at 2 K. The IRM increases as  $H_r$  increases from 30 to 40 kA/m, indicating that the increments in IRM correspond to

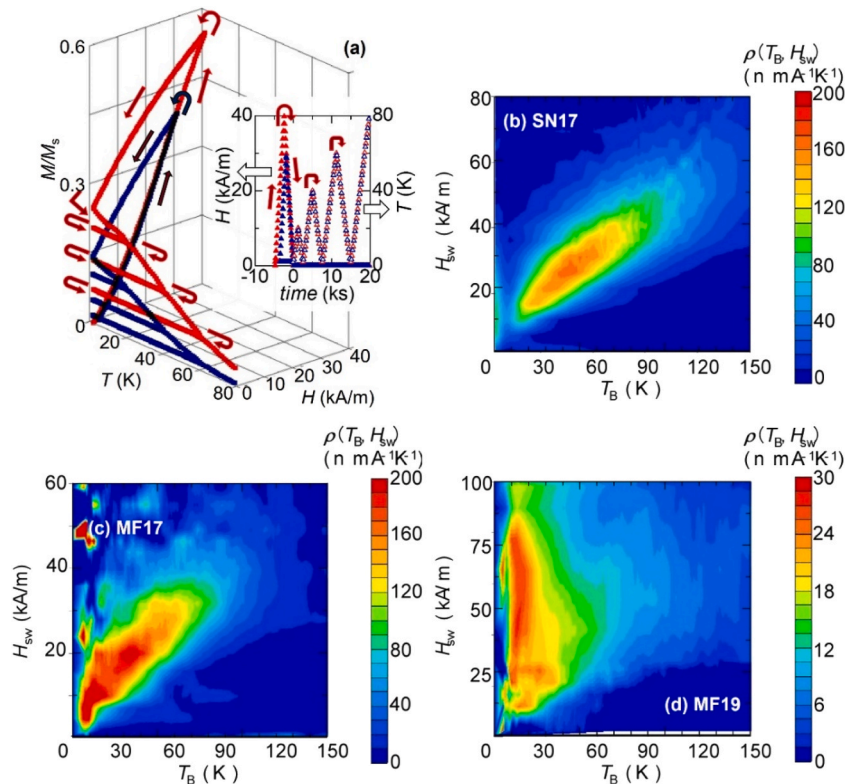


**Fig. 5.** Magnetic parameter distributions in magnetic nanoparticles. (a) Variations in isothermal remanent magnetization induced by magnetic field cycling and temporary heating. The inset shows the magnetic field and temperature sweep sequence. (b–d) Distributions of blocking temperature and switching magnetic field estimated for each nanoparticle sample.



the magnetization of nanoparticles with  $H_{SW}$  in this range. Accordingly, the  $H_{SW}$  distribution weighted by  $\mu$  can be estimated  $\frac{1}{M_s} \frac{\partial M(H_r)}{\partial H_r}$ , normalized by  $M_s = \sum_{all} \mu$ . Because the measurements were conducted near absolute zero, the extracted  $H_{SW}$  values correspond to  $H_{SW}(T \sim 0)$ , effectively free from thermal fluctuations.

Conversely, the IRM at zero magnetic field decreases due to random thermal fluctuations when the nanoparticles are heated to a higher temperature  $T_m$ . Once reduced by thermally activated reversal, the IRM does not recover upon subsequent cooling [91]. This behavior was confirmed for SN17, as shown in Fig. 5(a), where the particles were repeatedly heated and cooled while sequentially increasing the maximum temperature between 2 K and  $T_m = 20, 40$ , and 60 K at a sweep rate of 1 K/min.

Using this relationship, the distribution of  $T_B(t_m, H = 0)$  is typically estimated as  $-\frac{1}{M_s} \frac{\partial M(T_m)}{\partial T_m}$ . In relaxation experiments based on DC magnetization measurements, precise determination of  $t_m$  from the temperature sweep rate is difficult. However,  $t_m$  is commonly set to 100 s [91]. Based on the principles used in these two conventional analyses, we can identify that the thermal decay of IRM from  $T_m$  to  $T_m + \Delta T_m$  at  $H = 0$ , following temporary application of  $H_r$  at absolute zero, can be attributed only to particles satisfying the conditions  $T_m < T_B(t_m, H = 0) < T_m + \Delta T_m$  and  $H_{SW}(T = 0) < H_r$ . In other words, the joint  $T_B$ - $H_{SW}$ -distribution can be evaluated by combining the established  $T_B$ -distribution analysis derived from thermal decay curves with the conventional  $H_{SW}$ -distribution analysis based on remanent magnetization:

$$\rho(T_B, H_{SW}) = -\frac{1}{M_s} \frac{\partial^2 M(T_m, H_r)}{\partial T_m \partial H_r} \quad (9)$$

This method was recently proposed and has proven useful for analyzing realistic polydisperse nanoparticle systems [71]. It was, therefore, applied to SN17, and the resulting  $T_B(t_m, H = 0) - H_{SW}(T \sim 0)$

distribution map is shown in Fig. 5(b). This distribution extends along a diagonal line from the origin, consistent with theoretical expectations for single-domain nanoparticles, in which both  $T_B(t_m, H = 0)$  (or  $E_a(H = 0)$ ) and  $H_{SW}(T \sim 0)$  (or  $H_K$ ) scale with the intrinsic magnetic anisotropy constant, albeit with different proportionality factors.

Once the distribution of magnetic anisotropy barrier heights,  $E_a(H = 0) = k_B T_B(t_m, H = 0) \cdot \ln(t_m \cdot f_0)$ , and the corresponding distribution of switching fields,  $H_{SW}(T \sim 0) \propto H_K$ , has been determined, the magnetic response can be calculated using an appropriate model. This enables prediction of heat generation under irradiation conditions beyond the experimentally accessible range. In this study, a simple Preisach model [92] was employed, where the magnetization curve is computed as the sum of hysterons representing individual nanoparticles that reverse their magnetic moment  $\mu$  at their respective dynamical switching fields  $H_{SW}(T)$ . This model also accounts for probabilistic reversal induced by thermal fluctuations at finite temperatures using the empirical relation  $H_{SW}(T) \sim H_{SW}(T \sim 0) \cdot [1 - (T/T_B(t_m, H = 0))]^{0.77}$ . Because our objective is to evaluate hyperthermic performance at room temperature,  $SAR_{nano}$  at 300 K was calculated using  $k_B T_B \cdot \ln(f_0 \tau_m) = k_B (300 \text{ K}) \cdot \ln(f_0 / 2\pi f)$  derived from Eq. (6).

As shown in Fig. 6(a), the resulting  $SAR_{nano}/SAR_{max}$  map generated from the  $T_B$ - $H_{SW}$  distribution in Fig. 5(b) indicates that the heating efficiency index of SN17 increases with  $f$ , while its dependence on  $H_{ac}$  exhibits a peak at a specific amplitude, approximately 30 kA/m at  $f = 58 \text{ kHz}$ , as indicated by the cross section along the dashed line ( $f = 58 \text{ kHz}$ ) in the inset of Fig. 6(b).

Direct quantification of heat generated by the trace iron oxide cores within the silica shells was impractical due to lack of accuracy in determining the heat capacity and thermal conductivity of the silica coating. Therefore, we were unable to validate the prediction made above using the magnetic hyperthermia measurements. Instead, we measured the high-frequency, high-amplitude magnetization curves. As shown in Fig. 6(b), the resulting magnetization loop exhibits a distinct

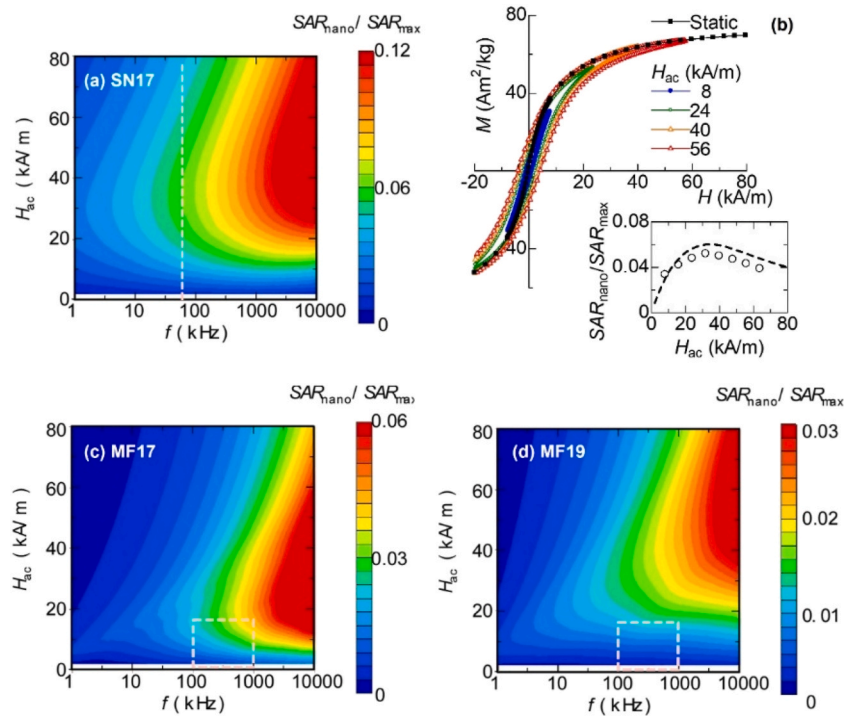


**Fig. 6.** Heating efficiency index  $SAR_{nano}/SAR_{max}$  of magnetic nanoparticles estimated from blocking temperature and switching-field distributions, shown as a function of irradiation frequency and magnetic field amplitude: (a) SN17, (c) MF17, and (d) MF19. The regions enclosed by white dashed lines in panels (c) and (d) represent the range in which the heating amount was directly measured experimentally. (b) Field-amplitude  $H_{ac}$  dependence of the dynamic magnetization curve measured for SN17 at  $f = 58 \text{ kHz}$ . The inset shows the cross-section along the dashed line ( $f = 58 \text{ kHz}$ ) in panel (a), together with  $SAR_{nano}/SAR_{max}$  estimated from the dynamic magnetization curves (denoted by white circles).

hysteresis. Using Eq. (2), the heat generation of SN17 was estimated from the hysteresis loop area. The values, plotted as open circles in the inset of Fig. 6(b), show good agreement with the calculated curve (broken line) derived from the  $T_B$ – $H_{SW}$  distribution in Fig. 5(b). This clearly demonstrates that the proposed method can reliably estimate  $SAR_{nano}/SAR_{max}$  of sparsely immobilized nanoparticles, as in SN17, after intracellular accumulation, under a remarkably wide range of irradiation conditions.

In contrast to such ideal systems, it should be recalled that magnetic nanoparticles used for therapy are administered as magnetic fluids and remain suspended in the blood or interstitial fluid, undergoing Brownian motion until they are taken up by cells. Furthermore, as mentioned earlier, magnetic nanoparticles can aggregate through various mechanisms, which can result in strong dipolar interactions between the nanoparticles. The proposed methodology was then applied to magnetic fluids MF17 and MF19, which serve as model systems for these effects. Fig. 5(c) presents the  $T_B(t_m, H=0)$ – $H_{SW}(T \sim 0)$  distribution map for MF17, obtained using the same procedure as for SN17. The distribution forms a diagonal line from the origin, similar to that observed for SN17, indicating behavior characteristic of magnetically isolated nanoparticles. This interpretation is consistent with the absence of detectable interaction fields in the FORC analysis of MF17 (see Supplementary Information). The result suggests that the particle size remains below the critical threshold for aggregation, preventing the formation of densely packed nanoparticle clusters in the bloodstream or interstitial fluids.

Fig. 6(c) presents the heating efficiency index  $SAR_{nano}/SAR_{max}$  maps derived from the  $T_B$ – $H_{SW}$  distribution in Fig. 5(c). For MF17, higher  $SAR_{nano}/SAR_{max}$  values are predicted at elevated frequencies beyond the experimental range of direct heating measurements, as indicated by the dashed lines. This trend is broadly consistent with the measured heating behavior of MF17 shown in Fig. 3(c), although quantitative discrepancies remain. To enable extrapolation based on this qualitative agreement, the estimated relative increase at higher frequencies was plotted after adjusting its absolute magnitude to match the experimental values, as shown by the solid blue line in Fig. 1(d). The results indicate that when the frequency is increased 20-fold, the  $SAR_{nano}/SAR_{max}$  ratio approximately doubles, as shown by the blue arrow in Fig. 1(d).

However, this increase occurs in the MHz range, which is significantly different from the frequencies (100 kHz, 310 kHz [80,81]) of alternating magnetic field devices currently used in clinical trials. While this initial screening is not intended to assess suitability for specific devices, it is important to note that increasing the frequency in MF17 causes the data point in Fig. 1(d) to move farther from the gray triangular region indicating practical requirements, as indicated by the blue arrow. In other words, the predicted improvement has no clinical significance for any type of hyperthermia device.

Next, we consider the MF19, for which the interaction field is non-negligible, as shown in the FORC diagram (see Supplementary Materials). Fig. 5(d) shows the  $T_B(t_m, H=0)$ – $H_{SW}(T \sim 0)$  distribution estimated using the same method applied to the other samples. In contrast to SN17 and MF17, the distribution for MF19 is concentrated in the low  $T_B$  region, and  $H_{SW}(T \sim 0)$  spans a wide range from 20 to 80 kA/m. In addition, a tail appears in the high  $T_B$ -region around 150 K at approximately  $H_{SW}(T \sim 0) \sim 50$  kA/m. These differences can be attributed to interparticle interactions in MF19.

Fig. 6(d) demonstrates the  $SAR_{nano}/SAR_{max}$  map for MF19 derived from the  $T_B$ – $H_{SW}$  distribution in Fig. 5(d). Larger  $SAR_{nano}/SAR_{max}$  values are predicted at larger magnetic field amplitudes beyond the measurement range, as indicated by the white dashed lines. This behavior is consistent with the general trend observed in the MF19 heating measurements shown in Fig. 3(d). For extrapolation, the estimated relative change with increasing field amplitude is plotted as a red solid line in Fig. 1(d), scaled to match the experimental values. According to this curve, doubling the magnetic field amplitude leads to a substantial increase in the heating efficiency index, although further increases are unlikely to yield additional gains. Unlike MF17, the MF19 showed a

tendency for the  $SAR_{nano}/SAR_{max}$  to temporarily approach practical target area, indicating that systematic measurements at higher field amplitudes are warranted for this class of nanoparticles.

However, a quantitative mismatch is observed between the predicted and measured values for MF17 and MF19, in contrast to the agreement obtained for the sparsely immobilized SN17 sample. Although the predicted trends with respect to irradiation conditions are qualitatively consistent, these discrepancies arise from applying a simplified model based solely on the Néel relaxation of magnetically isolated particles, as in SN17, to systems that also undergo Brownian rotation and exhibit interparticle interactions. Consequently, an extended model that incorporates these effects is required to achieve accurate quantitative predictions for nanoparticles dispersed in blood or interstitial fluid, as well as for aggregated nanoparticles. However, the current understanding of magnetic fluids, including their interaction dynamics and Brownian motion, remains insufficient to support such refinements. Further investigation of the fundamental properties of magnetic fluids is therefore necessary in future studies.

## 5. Conclusion

Magnetic fluid hyperthermia is a promising methodology for selective tumor treatment that exploits heat generated by magnetic nanoparticles under alternating magnetic fields. Conventional development of such nanoparticles has relied primarily on the specific absorption rate ( $SAR_{nano}$ ), a metric that depends strongly on the applied magnetic field amplitude and frequency. However, as irradiation conditions vary across studies and are often constrained by available instrumentation, comparisons based on  $SAR_{nano}$  are inherently limited and do not necessarily reflect the intrinsic heating efficiency of the nanoparticles. This study proposes and evaluates alternative performance indices and demonstrates that the ratio of experimentally obtained  $SAR_{nano}$  to its theoretical maximum provides an effective, condition-independent measure of intrinsic heating efficiency.

In addition, a methodology is introduced in this study to predict heating performance over a broad parameter range by jointly analyzing blocking-temperature and switching-field distributions. Application of this approach to silica-coated nanoparticle powders and two magnetic fluids is conducted and offers several insights. For sparsely immobilized iron oxide nanoparticles, such as those intracellularly accumulated with sufficient interparticle spacing, as a result of ideal single-particle endocytosis, the predicted heating efficiencies match the experimental measurements, confirming the method's ability to identify optimal irradiation conditions and estimate maximum heating capacity.

For model samples of nanoparticles with Brownian motion in blood or interstitial fluid, as well as that for aggregated nanoparticles exhibiting interparticle interactions, the predicted results were only in qualitative agreement with experimental trends. Extrapolating these relationships to predict irradiation conditions favorable for enhanced heating with enough reliability, further improvements that fully account for Brownian motion and interparticle interactions are considered necessary. In the future, as our understanding of magnetic fluids with significant interparticle interactions advances and the predictive accuracy of this approach for real, complex systems improves, it will help to prevent the premature exclusion of nanoparticle formulations that could exhibit high heating efficiencies under irradiation conditions beyond the practical limits of initial screening.

Overall, the efficiency metric and predictive framework proposed in this study are expected to contribute to building a more robust foundation for guiding the development of magnetic nanoparticles for hyperthermia applications.

## Author contributions

CRedit.

Hiroaki MAMIYA: Conceptualization, Methodology, Investigation,

Writing – original draft.

Balachandran JEYADEVAN: Methodology – synthesis, Investigation, Writing – review and editing.

Eiji KITA: Methodology – spectroscopy, Investigation, Writing – review and editing.

Reisho ONODER: Methodology – magnetometry, Investigation, Writing – review and editing.

Tetsushi TAGUCHI: Project administration, Investigation, Writing – review and editing.

Nikita KULESH: Software, Investigation, Writing – review and editing.

Hossein SEPEHRI AMIN: Project administration, Investigation, Writing – review and editing.

All authors have read and approved the final manuscript.

## Declaration of generative AI use

During the preparation of this work, the author(s) used NIMS Azure Chat in order to proofread the draft. After using this tool, the author(s) reviewed and edited the content as needed and take(s) full responsibility for the content of the publication.

## Funding

This work was partially supported by JSPS KAKENHI Grant No. 24K01305. A part of this work was supported by “Advanced Research Infrastructure for Materials and Nanotechnology in Japan (ARIM)” of the Ministry of Education, Culture, Sports, Science and Technology (MEXT) (Grant No. 24NM5119). The X-ray absorption near edge structure (XANES) spectroscopy was performed at the BL08W of NanoTerasu with the approval of PhoSIC (No. p0000002332).

## Declaration of competing interest

The authors declare that they have no known competing financial interests or personal relationships that could have appeared to influence the work reported in this paper.

## Acknowledgements

This work was partially supported by JSPS KAKENHI Grant No. 24K01305. It was also supported in part by the “Advanced Research Infrastructure for Materials and Nanotechnology in Japan (ARIM)” of the Ministry of Education, Culture, Sports, Science and Technology (MEXT) (Grant No. 24NM5119). X-ray absorption near-edge structure (XANES) spectroscopy was performed at BL08W of NanoTerasu with the approval of PhoSIC (No. p0000002332).

## Appendix A. Supplementary data

Supplementary data to this article can be found online at <https://doi.org/10.1016/j.mtnano.2026.100869>.

## Data availability

Data will be made available on request.

## References

- [1] Q.A. Pankhurst, N.K.T. Thanh, S.K. Jones, J. Dobson, Progress in applications of magnetic nanoparticles in biomedicine, *J. Phys. D Appl. Phys.* 42 (2009) 224001, <https://doi.org/10.1088/0022-3727/42/22/224001>.
- [2] K.M. Krishnan, Biomedical nanomagnetism: a spin through possibilities in imaging, diagnostics, and therapy, *IEEE Trans. Magn.* 46 (2010) 2523–2558, <https://doi.org/10.1109/TMAG.2010.2046907>.
- [3] S. Dutz, R. Hergt, Magnetic nanoparticle heating and heat transfer on a microscale: basic principles, realities and physical limitations of hyperthermia for tumour therapy, *Int. J. Hyperther.* 29 (2013) 790–800, <https://doi.org/10.3109/02656736.2013.822993>.
- [4] H. Mamiya, Recent advances in understanding magnetic nanoparticles in AC magnetic fields and optimal design for targeted hyperthermia, *J. Nanomater.* (2013) 752973, <https://doi.org/10.1155/2013/752973>.
- [5] H. Mamiya, B. Jeyadevan, Magnetic fluid hyperthermia; a guide for design of thermal seeds within the limits of conventional theory, in: Akinobu Yamaguchi, Atsufumi Hirohata, Bethanie J.H. Stadler (Eds.), *Nanomagnetic Materials Fabrication, Characterization and Application*, Elsevier, 2021, pp. 693–712, <https://doi.org/10.1016/C2018-0-05445-6>, 2021.
- [6] W. Andrä, C.G. d'Ambly, R. Hergt, I. Hilger, W.A. Kaiser, *J. Magn. Magn. Mater.* 194 (1999) 197–203, [https://doi.org/10.1016/S0304-8853\(98\)00552-6](https://doi.org/10.1016/S0304-8853(98)00552-6).
- [7] L. Shoshiashvili, I. Shamatava, D. Kakulia, F. Shubitidze, Design and assessment of a novel biconical human-sized alternating magnetic field coil for MNP hyperthermia treatment of deep-seated cancer, *Cancers* 15 (2023) 1672, <https://doi.org/10.3390/cancers15061672>.
- [8] J.F. Hainfeld, D.N. Slatkin, H.M. Smilowitz, The use of gold nanoparticles to enhance radiotherapy in mice, *Phys. Med. Biol.* 49 (2004) N309–N315, <https://doi.org/10.1088/0031-9155/49/18/N03>.
- [9] H.S. Huang, J.F. Hainfeld, Intravenous magnetic nanoparticle cancer hyperthermia, *Int. J. Nanomed.* 8 (2013) 2521–2532, <https://doi.org/10.2147/IJN.S43770>.
- [10] S.A. Rajan, N.K. Sahu, Inductive calorimetric assessment of iron oxide nano-octahedrons for magnetic fluid hyperthermia, *Colloids Surf. A Physicochem. Eng. Asp.* 603 (20 October 2020) 125210, <https://doi.org/10.1016/j.colsurfa.2020.125210>.
- [11] B. Mehdaoui, R.P. Tan, A. Meffre, J. Carrey, S. Lachaize, B. Chaudret, M. Respaud, Increase of magnetic hyperthermia efficiency due to dipolar interactions in low-anisotropy magnetic nanoparticles: theoretical and experimental results, *Phys. Rev. B* 87 (2013) 174419, <https://doi.org/10.1103/PhysRevB.87.174419>.
- [12] F. Shubitidze, K. Kekalo, R. Stigliano, I. Baker, Magnetic nanoparticles with high specific absorption rate of electromagnetic energy at low field strength for hyperthermia therapy, *J. Appl. Phys.* 117 (2015) 094302, <https://doi.org/10.1063/1.4907915>.
- [13] P.H. Linh, N.V. Chien, D.D. Dung, P.H. Nam, D.T. Hoa, N.T.N. Anh, L.V. Hong, N. X. Phuc, P.T. Phong, Biocompatible nanoclusters of O-carboxymethyl chitosan-coated Fe<sub>3</sub>O<sub>4</sub> nanoparticles: synthesis, characterization and magnetic heating efficiency, *J. Mater. Sci.* 53 (2018) 8887–8900, <https://doi.org/10.1007/s10853-018-2180-0>.
- [14] J.-T. Jang, J. Lee, J. Seon, E. Ju, M. Kim, Y.I. Kim, M.G. Kim, Y. Takemura, A. S. Arbab, K.W. Kang, K.H. Park, S.H. Paek, S. Bae, Giant magnetic heat induction of magnesium-doped  $\gamma$ -Fe<sub>2</sub>O<sub>3</sub> superparamagnetic nanoparticles for completely killing tumors, *Adv. Mater.* 30 (2018) 1704362, <https://doi.org/10.1002/adma.201806347>.
- [15] O.M. Lemine, A. Alanazi, E.L. Albert, M. Hjiri, M.O. M'hamed, S.A. Alrub, A. Alkaoud, C.A.C. Abdullah,  $\gamma$ -Fe<sub>2</sub>O<sub>3</sub>/Gd<sub>2</sub>O<sub>3</sub>-Chitosan magnetic nanocomposite for hyperthermia application: structural, magnetic, heating efficiency and cytotoxicity studies, *Appl. Phys. A* 126 (2020) 471, <https://doi.org/10.1007/s00339-020-03649-5>.
- [16] F.A. da Silva, M.F. de Campos, Study of heating curves generated by magnetite nanoparticles aiming application in magnetic hyperthermia, *Braz. J. Chem. Eng.* 37 (2020) 543–553, <https://doi.org/10.1007/s43153-020-00063-5>.
- [17] J.J. Ibarra-Sánchez, K.J. Delgado-Carrillo, A. Ceja-Fdz, D. Olivares-Vera, et al., Size control, chemical kinetics, and theoretical analysis for production of Fe<sub>3</sub>O<sub>4</sub> nanoparticles with a high specific absorption rate, *Ind. Eng. Chem. Res.* 59 (38) (2020) 16669–16683, <https://doi.org/10.1021/acs.iecr.0c02780>.
- [18] Z. Shaterabadi, G. Nabyouni, M. Soleymani, Correlation between effects of the particle size and magnetic field strength on the magnetic hyperthermia efficiency of dextran-coated magnetite nanoparticles, *Mater. Sci. Eng. C* 117 (2020) 111274, <https://doi.org/10.1016/j.msec.2020.111274>.
- [19] L. Storozhuk, M.O. Besenhard, S. Mourdikoudis, A.P. LaGrow, M.R. Lees, L. D. Tung, A. Gavrilidis, N.T.K. Thanh, Stable iron oxide nanoflowers with exceptional magnetic heating efficiency: simple and fast polyol synthesis, *ACS Appl. Mater. Interfaces* 13 (2021) 45870–45880, <https://doi.org/10.1021/acsami.1c12323>.
- [20] S.K. Shaw, J. Kailashiya, A. Gangwar, S.K. Alla, S.K. Gupta, C.L. Prajapat, S. Singh Meena, D. Dash, P. Maiti, N.K. Prasad,  $\gamma$ -Fe<sub>2</sub>O<sub>3</sub> nanoflowers as efficient magnetic hyperthermia and photothermal agent, *Appl. Surf. Sci.* 560 (2021) 150025, <https://doi.org/10.1016/j.apsusc.2021.150025>.
- [21] R. Das, J.A. Masa, V. Kalappattil, Z. Nemat, I. Rodrigo, E. Garaio, J.Á. García, M.-H. Phan, H. Srikanth, Iron oxide nanorings and nanotubes for magnetic hyperthermia: the problem of intraparticle interactions, *Nanomaterials* 11 (2021) 1380, <https://doi.org/10.3390/nano11061380>.
- [22] K. Vamvakidis, N. Maniotis, C. Dendrinos-Samara, Magneto-fluorescent nanocomposites: experimental and theoretical linkage for the optimization of magnetic hyperthermia, *Nanoscale* 13 (2021) 6426–6438, <https://doi.org/10.1039/D1NR00121C>.
- [23] R. Kumar, A. Chauhan, B.K. Kuanr, A robust in vitro anticancer activity via magnetic hyperthermia mediated by colloidal stabilized mesoporous silica encapsulated La<sub>0.7</sub>Sr<sub>0.3</sub>MnO<sub>3</sub> core-shell structure, *Colloids Surf. A Physicochem. Eng. Asp.* 615 (2021) 126212, <https://doi.org/10.1016/j.colsurfa.2021.126212>.
- [24] M.S.A. Darwish, H. Kim, M.P. Bui, T.-A. Le, H. Lee, C. Ryu, J. Young Lee, J. Yoon, The heating efficiency and imaging performance of magnesium iron oxide/tetramethyl ammonium hydroxide nanoparticles for biomedical applications, *Nanomaterials* 11 (2021) 1096, <https://doi.org/10.3390/nano11051096>.



- [25] M. Ortega-Muñoz, S. Plesselova, A.V. Delgado, F. Santoyo-Gonzalez, R. Salto-Gonzalez, M.D. Giron-Gonzalez, G.R. Iglesias, F.J. López-Jaramillo, Poly(ethyleneimine)-functionalized magnetite nanoparticles derivatized with folic acid: heating and targeting properties, *Polymers* 13 (2021) 1599, <https://doi.org/10.3390/polym13101599>.
- [26] S.R. Patade, D.D. Andhare, M.V. Khedkar, S.A. Jadhav, K.M. Jadhav, Editorial expression of concern: synthesis and characterizations of magnetically inductive Mn–Zn spinel ferrite nanoparticles for hyperthermia applications, *J. Mater. Sci. Mater. Electron.* 32 (2021) 13685–13692, <https://doi.org/10.1007/s10854-021-05946-y>.
- [27] I. Castellanos-Rubio, O. Arriortua, L. Marciano, I. Rodrigo, D. Iglesias-Rojas, A. Barón, A. Olazagoitia-Garmendia, L. Olivi, F. Plazaola, M.L. Fdez-Gubieda, A. Castellanos-Rubio, J.S. Garitaonandia, I. Orue, M. Insausti, Shaping up Zn-doped magnetite nanoparticles from mono- and bimetallic oleates: the impact of Zn content, Fe vacancies, and morphology on magnetic hyperthermia performance, *Chem. Mater.* 33 (2021) 3139–3154, <https://doi.org/10.1021/acs.chemmater.0c04794>.
- [28] Arunima Rajan, Niroj Kumar Sahu, Hydrophobic-to-Hydrophilic transition of Fe<sub>3</sub>O<sub>4</sub> nanorods for magnetically induced hyperthermia, *ACS Appl. Nano Mater.* 4 (5) (2021) 4642–4653, <https://doi.org/10.1021/acsanm.1c00274>.
- [29] J.B. Mamani, T.K.F. Souza, M.P. Nucci, F.A. Oliveira, L.P. Nucci, A.H. Alves, G.N. A. Rego, L. Marti, L.F. Gamarra, In vitro evaluation of hyperthermia magnetic technique indicating the best strategy for internalization of magnetic nanoparticles applied in glioblastoma tumor cells, *Pharmaceutics* 13 (2021) 1219, <https://doi.org/10.3390/pharmaceutics13081219>.
- [30] R. Gupta, D. Sharma, (Carboxymethyl-stevioside)-coated magnetic dots for enhanced magnetic hyperthermia and improved glioblastoma treatment, *Colloids Surf. B Biointerfaces* 205 (2021) 111870, <https://doi.org/10.1016/j.colsurfb.2021.111870>.
- [31] A. Rezaeezhad, A. Hajalilou, F. Eslami, E. Parvini, E. Abouzari-Lotf, B. Aslibeiki, Superparamagnetic magnetite nanoparticles for cancer cells treatment via magnetic hyperthermia: effect of natural capping agent, particle size and concentration, *J. Mater. Sci. Mater. Electron.* 32 (2021) 24026–24040, <https://doi.org/10.1007/s10854-021-06865-8>.
- [32] M. Cohen-Erner, R. Khandadash, R. Hof, O. Shalev, A. Antebi, A. Cyjon, D. Kanakov, A. Nyska, G. Goss, J. Hilton, D. Peer, Fe<sub>3</sub>O<sub>4</sub> nanoparticles and paraffin wax as phase change materials embedded in polymer matrices for temperature-controlled magnetic hyperthermia, *ACS Appl. Nano Mater.* 4 (2021) 11187–11198, <https://doi.org/10.1021/acsanm.1c02676>.
- [33] J. Gonçalves, C. Nunes, L. Ferreira, M.M. Cruz, H. Oliveira, V. Bastos, Á. Mayora, Q. Zhang, P. Ferreira, Coating of magnetite nanoparticles with fucoidan to enhance magnetic hyperthermia efficiency, *Nanomaterials* 11 (2021) 2939, <https://doi.org/10.3390/nano11112939>.
- [34] S. Shatooti, M. Mozaffari, G. Reiter, D. Zahn, S. Dutz, Heat dissipation in Sm<sup>3+</sup> and Zn<sup>2+</sup> co-substituted magnetite (Zn<sub>0.4</sub>Sm<sub>0.6</sub>Fe<sub>2.9</sub>O<sub>4</sub>) nanoparticles coated with citric acid and pluronic F127 for hyperthermia application, *Sci. Rep.* 11 (2021) 16795, <https://doi.org/10.1038/s41598-021-96238-2>.
- [35] I. Fizesan, C. Iacovita, A. Pop, B. Kiss, R. Dudric, C.M. Lucaciu, F. Loghin, The effect of Zn-substitution on the morphological, magnetic, cytotoxic, and in vitro hyperthermia properties of polyhedral ferrite magnetic nanoparticles, *Pharmaceutics* 13 (2021) 2148, <https://doi.org/10.3390/pharmaceutics13122148>.
- [36] C. Papadopoulos, A. Kolokithas-Ntoukas, R. Moreno, D. Fuentes, G. Loudos, V. C. Loukopoulos, G.C. Kagadis, *Med. Phys.* 49 (2022) 547–567, <https://doi.org/10.1002/mp.15317>.
- [37] P. Ghutepatil, V.M. Khot, A.B. Salunkhe, Design of monodispersed PVP functionalized biocompatible manganese ferrite nanoparticles for hyperthermia application, *Mater. Today Proc.* 62 (2022) 5341–5346, <https://doi.org/10.1016/j.matpr.2022.03.417>.
- [38] M. Vassallo, D. Martella, G. Barrera, F. Celegato, M. Coisson, R. Ferrero, E. S. Olivetti, A. Troia, H. Sözeri, C. Parmeggiani, D.S. Wiersma, P. Tiberto, A. Manzin, Improvement of hyperthermia properties of iron oxide nanoparticles by surface coating, *ACS Omega* 8 (2022) 2143–2154, <https://doi.org/10.1021/acsomega.2c06244>.
- [39] S. Shatooti, M. Mozaffari, G. Reiter, D. Zahn, S. Dutz, An investigation on the heat dissipation in Zn-substituted magnetite nanoparticles, coated with citric acid and pluronic F127 for hyperthermia application, *Physica B Condens. Matter* 625 (2022) 413468, <https://doi.org/10.1016/j.physb.2021.413468>.
- [40] K. El-Boubbou, O.M. Lemine, R. Ali, S.M. Huwaizi, S. Al-Humaida, A. AlKushia, Evaluating magnetic and thermal effects of various Polymerylated magnetic iron oxide nanoparticles for combined chemo-hyperthermia, *New J. Chem.* 46 (2022) 5489–5504, <https://doi.org/10.1039/D1NJ05791J>.
- [41] R. Kavkhani, A. Hajalilou, E. Abouzari-Lotf, L.P. Ferreira, et al., CTAB assisted synthesis of MnFe<sub>2</sub>O<sub>4</sub>@ SiO<sub>2</sub> nanoparticles for magnetic hyperthermia and MRI application, *Mater. Today Commun.* 31 (2022) 103412, <https://doi.org/10.1016/j.mtcomm.2022.103412>.
- [42] D. Ramirez, J. Oliva, T. Cordova-Fraga, G. Basurto-Islas, et al., High heating efficiency of magnetite nanoparticles synthesized with citric acid: application for hyperthermia treatment, *J. Electron. Mater.* 5 (2022) 4425–4436, <https://doi.org/10.1007/s11664-022-09678-5>.
- [43] A.G. González, N. Casillas, Z. López, O. Cervantes, P. Knauth, R. Hernández-Gutiérrez, A. Topete-Camacho, S. Rosales, L.H. Quintero, J.A. Paz, X. Flores, M. E. Cano, Tetrahydroxyquinone: a suitable coating for ferrofluids used in magnetic hyperthermia, *Coatings* 12 (2022) 1130, <https://doi.org/10.3390/coatings12081130>.
- [44] M. Mirković, Z. Milanović, M. Perić, S. Vranješ-Durić, M. Ognjanović, B. Antić, M. Kuraica, I. Krstić, M. Kubovcikov, I. Antal, R. Sobotova, V. Zavisova, A. Jurikova, M. Fabian, M. Koneracka, Design and preparation of proline, tryptophan and poly-L-lysine functionalized magnetic nanoparticles and their radiolabeling with <sup>131</sup>I and <sup>177</sup>Lu for potential theranostic use, *Int. J. Pharmaceutics* 628 (2022) 122288, <https://doi.org/10.1016/j.ijpharm.2022.122288>.
- [45] V. Narayanaswamy, J. Jagal, H. Khurshid, I.A. Al-Omari, M. Haider, A.S. Kamzin, I. M. Obaidat, B. Issa, Hyperthermia of magnetically soft-soft core-shell ferrite nanoparticles, *Int. J. Mol. Sci.* 23 (2022) 14825, <https://doi.org/10.3390/ijms232314825>.
- [46] X. Yu, T. Yang, R. Liu, D. Wu, D. Tian, T. Zhou, H. Yan, S. He, H. Zeng, Simultaneous enhancement of magnetothermal and photothermal responses by Zn, Co co-doped ferrite nanoparticles, *Small* 18 (2022) 2205037, <https://doi.org/10.1002/sml.202205037>.
- [47] V. Vinodhini, K. Chintagumpala, Superparamagnetic hyperthermia and cytotoxicity properties of bimagnetic core-shell nanoparticles synthesized by solvothermal reflux method, *J. Magn. Magn Mater.* 565 (2023) 170290, <https://doi.org/10.1016/j.jmmm.2022.170290>.
- [48] A. Singh, P. Kumar, S. Pathak, K. Jain, P. Garg, M. Pant, A.K. Mahapatro, D. Rath, L. Wang, S.-K. Kim, K.K. Maurya, R.P. Pant, A threefold increase in SAR performance for magnetic hyperthermia by compositional tuning in zinc-substituted iron oxide superparamagnetic nanoparticles with superior biocompatibility, *J. Alloys Compd.* 968 (2023) 171868, <https://doi.org/10.1016/j.jallcom.2023.171868>.
- [49] M.A. Kashi, K. Heydaryan, A comparative study on characterization and hyperthermia properties of CoFe<sub>2</sub>O<sub>4</sub> nanoparticles synthesized with different surfactants, *J. Mater. Sci. Mater. Electron.* 34 (2023) 2255, <https://doi.org/10.1007/s10854-023-11676-0>.
- [50] S.J. Olusegun, M. Osial, A. Majkowska-Pilip, K. Żelechowska-Matysiak, D. Nieciecka, M. Krajewski, M. Pekała, P. Kryszewski, Synthesis and characterization of Sr<sup>2+</sup> and Gd<sup>3+</sup> doped magnetite nanoparticles for magnetic hyperthermia and drug delivery application, *Ceram. Int.* 49 (2023) 19851–19860, <https://doi.org/10.1016/j.ceramint.2023.03.102>.
- [51] A.M. Nowicka, M. Ruzicka-Ayoush, A. Kasprzak, A. Kowalczyk, M. Bamburowicz-Klimkowska, M. Sikorska, K. Sobczak, M. Dönten, A. Ruszczyńska, J. Nowakowska, I.P. Grudziński, Application of biocompatible and ultrastable superparamagnetic iron(III) oxide nanoparticles doped with magnesium for efficient magnetic fluid hyperthermia in lung cancer cells, *J. Mater. Chem. A* 11 (2023) 4028–4041, <https://doi.org/10.1039/D3TB00167A>.
- [52] Raji R. Krishnan, E. Prasad, Francis Boniface Fernandez, K.V. Nishad, Shine R. Chandran, Elizabeth Johnson, K.H. Prema, Hyperthermia heating efficiency of glycine functionalised graphene oxide modified nickel nanoparticles, *J. Alloys Compd.* 982 (2024) 173804, <https://doi.org/10.1016/j.jallcom.2024.173804>.
- [53] Y. Iqbal, W.H. Shah, M.Y. Khan, P. Ahmed, M.T. Qureshi, A.M. Khaled, M.S. Salem, Optimizing the magnetic field strength and concentration of silica coated cobalt ferrite nanoparticles for magnetic hyperthermia, *Inorg. Chem. Commun.* 167 (2024) 12796, <https://doi.org/10.1016/j.inoche.2024.12796>.
- [54] N. Van Khien, C.T.A. Xuan, L.H. Nguyen, P.H. Nam, T.T. Thao, Role of citric acid coating in enhancing applicability of CoFe<sub>2</sub>O<sub>4</sub> nanoparticles in antibacterial and hyperthermia, *Mater. Today Commun.* 38 (2024) 107982, <https://doi.org/10.1016/j.mtcomm.2023.107982>.
- [55] M. Lázaro, Á.V. Delgado, G.R. Iglesias, Magneto-photothermal synergy applied to gold-coated magnetic nanoparticles, *J. Magn. Magn Mater.* 591 (2024) 171718, <https://doi.org/10.1016/j.jmmm.2024.171718>.
- [56] G. Soares da Silva, A. Aparecida de Almeida, F. Fabris, D. Muraca, Investigating unusual dynamics: time and frequency-dependent variations in specific power absorption of magnetite nanoparticles in magnetic hyperthermia, 2024 IEEE International Magnetic Conference – Short Papers (INTERMAG Short Papers), 1–2.
- [57] Y. Ying, Y. Zhou, J. Yu, L. Qiao, J. Zheng, W. Li, J. Li, S. Che, Preparation of dextran- and carboxymethyl dextran-coated Fe<sub>3</sub>O<sub>4</sub> nanoparticles for breast cancer cell labeling and magnetic hyperthermia, *Nanotheranostics* 8 (2024) 442–457, <https://doi.org/10.1007/s10948-024-06788-5>.
- [58] C. Martins, C. Rolo, V.R.G. Cacho, L.C.J. Pereira, J.P. Borges, J. Carvalho Silva, T. Vieira, P.I.P. Soares, Enhancing the magnetic properties of superparamagnetic iron oxide nanoparticles using hydrothermal treatment for magnetic hyperthermia application, *Mater. Adv.* 6 (2025) 1726–1743, <https://doi.org/10.1039/D4MA01120A>.
- [59] Silvio Dutz, Melanie Kettering, Ingrid Hilger, Robert Muller, Matthias Zeisberger, Magnetic multicore nanoparticles for hyperthermia – influence of particle immobilization in tumour tissue on magnetic properties, *Nanotechnology* 22 (2011) 265102, <https://doi.org/10.1088/0957-4484/22/26/265102>.
- [60] J. Kolosnjaj-Tabi, R. Di Corato, L. Lartigue, I. Marangon, P. Guardia, A.K.A. Silva, N. Luciani, O. Clément, P. Flaud, J.V. Singh, P. Decuzzi, T. Pellegrino, C. Wilhelm, F. Gazeau, Heat-generating iron oxide nanocubes: subtle “deconstructors” of the tumoral microenvironment, *ACS Nano* 8 (2014) 4268–4283, <https://doi.org/10.1021/nl405356r>.
- [61] R. Di Corato, A. Espinosa, L. Lartigue, M. Tharaud, S. Chat, T. Pellegrino, C. Ménager, F. Gazeau, C. Wilhelm, Magnetic hyperthermia efficiency in the cellular environment for different nanoparticle designs, *Biomaterials* 35 (2014) 6400–6411, <https://doi.org/10.1016/j.biomaterials.2014.04.036>.
- [62] D. Soukup, S. Moise, E. Céspedes, J. Dobson, N.D. Telling, *In Situ* measurement of magnetization relaxation of internalized nanoparticles in live cells, *ACS Nano* 9 (2015) 231–240, <https://doi.org/10.1021/nl503888j>.
- [63] K. Hiroi, K. Komatsu, T. Sato, Superspin glass originating from dipolar interaction with controlled interparticle distance among γ-Fe<sub>2</sub>O<sub>3</sub> nanoparticles with silica

- shells, *Phys. Rev. B* 83 (2011) 224423, <https://doi.org/10.1103/PhysRevB.83.224423>.
- [64] H. Mamiya, H. Fukumoto, J.L.C. Huaman, K. Suzuki, H. Miyamura, J. Balachandran, Estimation of magnetic anisotropy of individual magnetite nanoparticles for magnetic hyperthermia, *ACS Nano* 14 (2020) 8421, <https://doi.org/10.1021/acsnano.0c02521>.
- [65] H. Mamiya, I. Furukawa, J.L. Cuya Huaman, K. Suzuki, H. Miyamura, B. Jeyadevan, Evaluation of interparticle interactions between magnetic nanoparticles using first order reversal curves and weiss temperature, *J. Phys. Commun.* 5 (2021) 045003, <https://doi.org/10.1088/2399-6528/abee31>.
- [66] P. García-Acevedo, M.A. González-Gómez, Á. Armosa-Prieto, L. de Castro-Alves, Y. Piñeiro, J. Rivas, Role of dipolar interactions on the determination of the effective magnetic anisotropy in iron oxide nanoparticles, *Adv. Sci. (Weinh.)* 10 (2023) 2203397, <https://doi.org/10.1002/adv.202203397>.
- [67] H. Mamiya, I. Nakatani, T. Furubayashi, Phase transitions of iron-nitride magnetic fluids, *Phys. Rev. Lett.* 84 (2000) 6106, <https://doi.org/10.1103/PhysRevLett.84.6106>.
- [68] J.G. Ovejero, D. Cabrera, J. Carrey, T. Valdivielso, G. Salas, F.J. Teran, Effects of inter- and intra-aggregate magnetic dipolar interactions on the magnetic heating efficiency of iron oxide nanoparticles, *Phys. Chem. Chem. Phys.* 18 (2016) 10954, <https://doi.org/10.1039/C6CP00468G>.
- [69] N.A. Usov, O.N. Serebryakova, V.P. Tarasov, Interaction effects in assembly of magnetic nanoparticles nanoscale, *Nanoscale Res. Lett.* 12 (2017) 489, <https://doi.org/10.1186/s11671-017-2263-x>.
- [70] P.C. Scholten, How magnetic can a magnetic fluid be? *J. Magn. Magn. Mater.* 39 (1983) 99, [https://doi.org/10.1016/0304-8853\(83\)90409-2](https://doi.org/10.1016/0304-8853(83)90409-2).
- [71] H. Mamiya, H. Sudo, J.L.C. Huaman, K. Suzuki, H. Miyamura, J. Balachandran, Macroscopic and microscopic structural analyses of needle-shaped condensed phases in magnetic fluids under external magnetic fields, *J. Phys. Chem. C* 125 (2021) 740, <https://doi.org/10.1021/acs.jpcc.0c08648>.
- [72] H. Gavilán, K. Simeonidis, E. Myrovali, E. Mazarío, O. Chubykalo-Fesenko, R. Chantrell, L. Balcells, M. Angelakeris, M.P. Morales, D. Serantes, How size, shape and assembly of magnetic nanoparticles give rise to different hyperthermia scenarios, *Nanoscale* 13 (2021) 15631–15646, <https://doi.org/10.1039/D1NR03484G>.
- [73] R. Hergt, R. Hiergeist, M. Zeisberger, D. Shuler, U. Heyen, I. Hilger, W. Kaiser, Magnetic properties of bacterial magnetosomes as diagnostics and therapeutic tools, *J. Magn. Magn. Mater.* 293 (2005) 80–86, <https://doi.org/10.1016/j.jmmm.2005.01.047>.
- [74] E. Myrovali, K. Papadopoulos, I. Iglesias, M. Spasova, M. Farle, U. Wiedwald, M. Angelakeris, Long-range ordering effects in magnetic nanoparticles, *ACS Appl. Mater. Interfaces* 13 (2021) 21602–21612, <https://doi.org/10.1021/acsaami.1c01820>.
- [75] R.A. Harris, P.M. Shumbula, H. Walt, Analysis of the interaction of surfactants oleic acid and oleylamine with iron oxide nanoparticles through molecular mechanics modeling, *Langmuir* 31 (2015) 3934–3943, <https://doi.org/10.1021/acs.langmuir.5b00671>.
- [76] Zhichuan Xu, Chengmin Shen, Yanglong Hou, Hongjun Gao, Shouheng Sun, Oleylamine as both reducing agent and stabilizer in a facile synthesis of magnetite nanoparticles, *Chem. Mater.* 21 (2009) 1778–1780, <https://doi.org/10.1021/cm802978z>.
- [77] K. Taguchi, I. Laakso, K. Aga, A. Hirata, Y. Diao, J. Chakrothai, Relationship of external field strength with local and whole-body averaged specific absorption rates in anatomical human models, *IEEE Access* 6 (2018) 70186, <https://doi.org/10.1109/ACCESS.2018.2880905>.
- [78] The International Commission on Non-Ionizing Radiation Protection (ICNIRP), Guidelines for limiting exposure to electromagnetic fields (100 KHz TO 300 GHz), *Health Phys.* 118 (2020) 483–524, <https://doi.org/10.1097/HP.0000000000001210>.
- [79] W.J. Atkinson, I.A. Brezovich, D.P. Chakraborty, Useable frequencies in hyperthermia with thermal seeds, *IEEE Trans. Biomed. Eng.* 31 (1984) 70–75, <https://doi.org/10.1109/TBME.1984.325372>.
- [80] K. Maier-Hauff, R. Rothe, R. Scholz, et al., Intracranial thermotherapy using magnetic nanoparticles combined with external beam radiotherapy: results of a feasibility study on patients with glioblastoma multiforme, *J. Neuro. Oncol.* 81 (2007) 53–60, <https://doi.org/10.1007/s11060-006-9195-0>.
- [81] Sarah Kraus, Boaz Shalev, Shir Arbib, Pazit Rukenstein, Moshe Eltanani, Udi Ron, Shaul Atar, Ofer Shalev, Tumor necrosis in a breast cancer case as a result of a novel systemic magnetic nanoparticle hyperthermia "Firstin-Human" safety and feasibility trial, *J. Clin. Case Rep.* 14 (2024) 2, <https://doi.org/10.37421/2165-7920.2024.14.1596>.
- [82] U. Gneveckow, A. Jordan, R. Scholz, V. Brühl, N. Waldöfner, J. Ricke, A. Feussner, B. Hildebrandt, B. Rau, P. Wust, Description and characterization of the novel hyperthermia-and thermoablation-system for clinical magnetic fluid hyperthermia, *Med. Phys.* 31 (2004) 1444–1451, <https://doi.org/10.1118/1.1748629DigitalObjectIdentifier>.
- [83] <https://www.resonantcircuits.com/news/rci-amp-vall-dhebron-enrolls-first-patient-for-treatment-of-pancreatic-cancer>.
- [84] A. Ito, T. Kobayashi, Intracellular hyperthermia using magnetic nanoparticles : a novel method for hyperthermia clinical applications, *Thermal Medicine* 24 (2008) 113–129, <https://doi.org/10.3191/thermalm.24.113>.
- [85] M. Suto, Y. Hirota, H. Mamiya, A. Fujita, R. Kasuya, K. Tohji, B. Jeyadevan, Heat dissipation mechanism of magnetite nanoparticles in magnetic fluid hyperthermia, *J. Magn. Magn. Mater.* 321 (2009) 1493, <https://doi.org/10.1016/j.jmmm.2009.02.070>.
- [86] M. Kallumadil, M. Tada, T. Nakagawa, M. Abe, P. Southern, Q.A. Pankhurst, Suitability of commercial colloids for magnetic hyperthermia, *J. Magn. Magn. Mater.* 321 (2009) 1509, <https://doi.org/10.1016/j.jmmm.2009.02.075>.
- [87] R.E. Rosensweig, Heating magnetic fluid with alternating magnetic field, *J. Magn. Magn. Mater.* 252 (2002) 370–374, [https://doi.org/10.1016/S0304-8853\(02\)00706-0](https://doi.org/10.1016/S0304-8853(02)00706-0).
- [88] A. Bordet, R.F. Landis, Y. Lee, G.Y. Tonga, J.M. Asensio, C.-H. Li, P.-F. Fazzini, K. Soulatia, V.M. Rotello, B. Chaudret, Water-dispersible and biocompatible iron carbide nanoparticles with high specific absorption rate, *ACS Nano* 13 (2019) 2870–2878, <https://doi.org/10.1021/acsnano.8b05671>.
- [89] W.F. Brown, Thermal fluctuations of a single-domain particle, *Phys. Rev.* 130 (1963) 1677, <https://doi.org/10.1103/PhysRev.130.1677>.
- [90] H. Pfeiffer, Determination of anisotropy field distribution in particle assemblies taking into account thermal fluctuations, *Phys. Status Solidi A* 118 (1990) 295–306, <https://doi.org/10.1002/pssa.2211180133>.
- [91] J.L. Dormann, D. Fiorani, *Magnetic Properties of Fine Particles*, first ed., Elsevier, Amsterdam, 1991.
- [92] F. Preisach, Über die magnetische nachwirkung, *Z. Phys.* 94 (1935) 277–302, <https://doi.org/10.1007/BF01349418>.